

Numerical modeling of self-limiting and self-enhancing caprock alteration induced by CO₂ storage in a depleted gas reservoir

Fabrizio Gherardi^{1,*}, Tianfu Xu² and Karsten Pruess²

¹ Istituto di Geoscienze e Georisorse (IGG) – Consiglio Nazionale delle Ricerche (CNR), 56124 Pisa, Italy

² Earth Sciences Division, Lawrence Berkeley National Laboratory, Berkeley, CA 94720

* Corresponding author. Tel.: +39 050 315 3409; fax: +39 050 315 2322; *E-mail address*: f.gherardi@igg.cnr.it

Abstract

This paper presents numerical simulations of reactive transport which may be induced in the caprock of an on-shore depleted gas reservoir by the geological sequestration of carbon dioxide. The objective is to verify that CO₂ geological disposal activities currently being planned for the study area are safe and do not induce any undesired environmental impact.

In our model, fluid flow and mineral alteration are induced in the caprock by penetration of high CO₂ concentrations from the underlying reservoir, where it was assumed that large amounts of CO₂ have already been injected at depth. The main focus is on the potential effect of precipitation and dissolution processes on the sealing efficiency of caprock formations. Concerns that some leakage may occur in the investigated system arise because the seal is made up of potentially highly-reactive rocks, consisting of carbonate-rich shales (calcite+dolomite averaging up to more than 30% of solid volume fraction). Batch simulations and multi-dimensional 1D and 2D modeling have been used to investigate multicomponent geochemical processes. Numerical simulations account for fracture-matrix interactions, gas

phase participation in multiphase fluid flow and geochemical reactions, and kinetics of fluid-rock interactions.

The geochemical processes and parameters to which the occurrence of high CO₂ concentrations are most sensitive are investigated by conceptualizing different mass transport mechanisms (i.e. diffusion and mixed advection+diffusion). The most relevant mineralogical transformations occurring in the caprock are described, and the feedback of these geochemical processes on physical properties such as porosity is examined to evaluate how the sealing capacity of the caprock could evolve in time.

The simulations demonstrate that the occurrence of some gas leakage from the reservoir may have a strong influence on the geochemical evolution of the caprock. In fact, when a free CO₂-dominated phase migrates into the caprock through fractures, or through zones with high initial porosity possibly acting as preferential flow paths for reservoir fluids, low pH values are predicted, accompanied by significant calcite dissolution and porosity enhancement. In contrast, when fluid-rock interactions occur under fully liquid-saturated conditions and a diffusion-controlled regime, pH will be buffered at higher values, and some calcite precipitation is predicted which leads to further sealing of the storage reservoir.

Keywords: CO₂ geological storage, caprock sealing, reactive chemical transport modelling

1. Introduction

Geologic sequestration is being considered as an effective means for reducing atmospheric emissions of CO₂. Modeling studies have suggested that under favorable conditions CO₂ can be confined for very long times (up to several thousand of years; see, among others, Bachu et al., 1994, Weir et al., 1996a, 1996b, Hitchon, 1996, White et al., 2005). Despite the great potential benefits of geologic sequestration, primarily because the CO₂ injected in the subsurface can be isolated from the atmosphere for long time periods, risks may nevertheless be present. In particular, CO₂ can leak from storage reservoirs and return to the atmosphere. This is because additional geochemical processes may take place as a consequence of dissolution of supercritical CO₂ into deep brines, which may affect the integrity of the carbon repository (e.g. Gunter et al., 2000). Leakage may occur through fractures, faults or, more generally, caprock weaknesses which may act as preferential ascent routes for deep-seated gases (Ennis-King and Paterson, 2000, Pruess and Garcia, 2002, Rutqvist and Tsang, 2002).

Experimental, modelling and field studies evaluating structural integrity of geological carbon repositories have been already conducted (see, among others, Li et al., 2006, Kaszuba et al., 2003, 2005, Gaus et al., 2005, Haszeldine et al., 2005, May, 2005, Marschall et al., 2005, Moore et al., 2005, Hildebrand et al., 2004, Pruess and Garcia, 2002, Rutqvist and Tsang, 2002, Ennis-King and Paterson, 2000, Lindeberg, 1997, and references cited therein). From these studies, the following key issues can be identified, which need to be addressed for a quantitative assessment of the sealing efficiency of caprock formations:

(i) to gain a better understanding of the fluid flow and geochemical processes that would accompany CO₂ migration from a storage reservoir towards shallow depths, it is crucial to

explore and evaluate the impacts of dissolution processes of caprock formations by acidic CO₂-rich fluids;

(ii) reactions induced by CO₂ in rocks filled with brackish or saline waters likely involve acid hydrolysis of rock-forming minerals. Dissolution reactions are likely when gas breakthrough is expected in carbonate-rich rocks, with both the type and timing of the mineralogical alteration in caprocks being highly variable and specific to geochemical, physical and hydrologic features of the investigated systems;

(iii) the sealing capacity of caprock formations above depleted oil and/or gas reservoirs can be significantly reduced after CO₂ injection, due to the lower interfacial tension of the CO₂-water system in comparison to hydrocarbon-water system originally filling the reservoir before the displacement operated by the injected CO₂ (Li et al., 2006);

(iv) experimental data on capillary displacement pressure and effective permeability-capillary pressure relationships indicate that dynamic leakage of gases through the caprock depends on ambient pressure conditions; differences in gas breakthrough behaviour of gases are governed by interfacial tension and wettability behaviour of different gases which are specific to different lithologies (Hildebrand et al., 2004);

(v) natural analogues provide useful information on geochemical processes occurring in natural environments that laboratory experiments may not be able to reproduce. Such information can assist in the calibration of geochemical models, allowing them to make accurate predictions at the timescales involved in nature (Haszeldine et al., 2005).

This paper is focused on the study of the reactive mechanisms which may occur as a consequence of CO₂ geological disposal at depth in a potentially highly-reactive caprock, consisting of carbonate-rich shales.

The site investigated here is a depleted on-shore gas reservoir in the North of Italy (Calabrese et al., 2005), in which prefeasibility studies have already identified favorable conditions for CO₂ injection and underground storage. The reservoir consists of a multilayered sandstone-shale formation located at depths generally below 1400 m b.g.l. (below ground level); simulations address the uppermost layer of this reservoir, where CO₂ injection is currently planned.

Available site-specific data include basic physical parameters (temperature, pressure, porosity, permeability, see section 6), chemical composition of reservoir aqueous solution, and caprock and reservoir mineralogy. The chemical composition of the caprock pore water is unknown, and has been inferred by batch modeling (see below).

Gas-water-rock interactions resulting from CO₂ migration into the caprock have been simulated under dominance of two alternative mass transport conditions: diffusion in the aqueous phase, and gas and/or liquid advection. All simulations concern the geological disposal of an almost pure-CO₂ waste stream. The effects induced by the underground disposal of less pure waste streams, as expected for coal-fired power plants where SO_x, NO_x, and H₂S gas species may be present along with CO₂ (Knauss et al., 2005), are not accounted for.

The simulations focus on CO₂-driven fluid-rock interactions in either sealed or fractured caprock. Field conditions are believed to be close to the “sealed caprock model”. An alternative fractured caprock model has been used to investigate the geochemical behavior of

the system under particularly severe conditions which are not currently encountered in the field, and to explore a hypothetical maximum risk scenario.

Major evidence supporting the assumption of a sealed caprock stems from the fact that no gas leakages have been detected during the exploitation phase, or in the course of subsequent reservoir repressurization due to the ingress of a laterally offset aquifer, and during several cycles of gas storage in the latest phase of reservoir management.

An extensive program of multidisciplinary laboratory tests on rock properties, geochemical and microseismic monitoring, and reservoir simulation studies is underway to better characterize the reservoir and cap-rock behavior before proceeding with a CO₂ sequestration pilot test.

Fluid-rock interactions in sealed caprock have been modeled through a series of simplified 1D models, consisting of 20 to 50 m long vertical sections of 1 m² cross-sectional area through the caprock. Fluid-rock interactions in fractured caprock have been modeled through a series of simplified 2D models, which consider idealized fractured rocks with single or multiple vertical fracture zones of variable aperture and spacing.

The gas-water-rock interactions occurring in the caprock are modeled under different reservoir gas saturation initial conditions. Low-gas initial conditions (i.e. $S_{g,RESERVOIR}$ typically between 0 to 0.5 in our simulations) are representative of conditions likely to occur in the peripheral zones of the field, where depressurization from past gas production has favored the inflow of local groundwaters, and aqueous phase is expected to only be partially or not

displaced by the gas plume. In this part of the field, the most relevant mineralogical changes occur in the aqueous phase, at the interface between reservoir and caprock formations.

High-gas initial conditions ($S_{g,RESERVOIR}$ typically between 0.7 to 0.9) are considered representative of conditions expected near the injection wells and in the inner parts of the CO₂ plume. In this case, major geochemical transformations occur at the advancing gas front.

All calculations were performed with the TOUGHREACT code, a comprehensive, publicly available reactive transport simulator for multiphase systems (Xu et al., 2004a). The numerical model was developed by introducing reactive chemistry into the framework of the existing multiphase and heat flow simulator TOUGH2 (Pruess, 1991, Pruess et al., 1999). Space discretization is obtained by means of an integral finite difference approach (Narasimhan and Witherspoon, 1976). Flow, transport, and geochemical reaction equations are solved separately by means of a sequential iteration approach similar to Yeh and Tripathi (1991). Full details on numerical methods are given in Xu and Pruess (1998) and Xu et al. (2001).

2. Modeling approach

Model development has been carried out in stages of increasing complexity. Starting from chemically, hydrologically and geometrically simplified systems, the sensitivity of system behavior has been explored with respect to parameters like grid geometry, initial mineralogy

and chemical composition of formation waters. Simulations have been carried out for a range of conditions, with mass transport dominated by diffusion or advection.

Variable time and space discretizations have been applied as a function of specific duration and detail of the simulations. Maximum simulation times vary from 10 to 1,000 years for 1D and 2D simulations, while the lower limit of the spatial resolution spans the range 0.001 to 0.1 m.

Calculations have been carried out under the local equilibrium assumption for aqueous complexation, acid-base, redox and gas dissolution/exolution reactions. The geochemical system is represented by means of a selected subset of aqueous species (Table 1) called “basis” species (or “component” or “primary” species). All other species (aqueous complexes, minerals and gaseous species) are called “secondary” species (Reed, 1982; Yeh and Tripathi, 1991; Steefel and Lasaga, 1994). The concentrations of aqueous complexes (Table 1) are expressed as functions of the concentrations of the basis species (Parkhurst et al., 1980; Reed, 1982), according to the following equation:

$$c_{complex_i} = K_i^{-1} \times \gamma_i^{-1} \times \prod_{j=1}^{N_{basis}} c_{basis_j}^{v_{ij}} \times \gamma_j^{v_{ij}} \quad [1]$$

where $c_{complex_i}$ and c_{basis_j} are molal concentration of the i-th aqueous complex and of the j-th basis species, respectively, γ_i and γ_j the thermodynamic activity coefficients, K_i the equilibrium constant, v_{ij} the stoichiometric coefficients of j-th basis species involved in the mass balance equation written for the i-th aqueous complex.

Aqueous activity coefficients are computed using an extended Debye-Hückel equation, according to Helgeson et al. (1981) and Tanger and Helgeson (1988).

Fugacity coefficients are computed for H₂O_(g) and CO_{2(g)} species by means of the virial equation of Spycher and Reed (1988).

Precipitation and dissolution of minerals are kinetically-controlled. The kinetic laws used here are derived from transition state theory (Lasaga, 1984). Effective reaction rates can be expressed through the following general equation:

$$rate = A_m \times k_m \times \left\{ 1 - \left(\frac{Q}{K} \right)^\mu \right\}^\eta \quad [2]$$

where A_m is the specific surface area, k_m is the kinetic rate constant, Q is the ion activity product, K the equilibrium constant for the specific mineral-water reaction, μ and η two constants which depend on experimental data; they are usually but not always taken equal to 1.

Kinetic rates may depend on pH and also on concentrations of non-basis species. The temperature dependence of the reaction rate constant is expressed via an Arrhenius equation:

$$k_m = k_{25} \times \exp \left[\frac{-E_a}{R} \times \left(\frac{1}{T} - \frac{1}{298.15} \right) \right] \quad [3]$$

where E_a is the activation energy, k_{25} is the rate constant at 25 deg-C, R is the gas constant, and T is absolute temperature.

The precipitation of a mineral can be suppressed up to a given, positive saturation index value. Within this "supersaturation window", the mineral is not allowed to precipitate.

However, due to the lack of reliable data potentially constraining this parameter, we did not use this option and we preferred to allow each saturated and/or supersaturated mineral to automatically start to precipitate. The initial effective surface area of each mineral not present at the start of a simulation is calculated as equivalent to those of sphere with radius 10^{-5} m (Xu et al, 2004a).

Porosity changes are directly tied to the volume changes as a result of mineral precipitation and dissolution, and these changes are taken into account in the calculations. The porosity of the medium is calculated with the following relationship:

$$\phi = 1 - \sum_{m=1}^{nm} fr_m - fr_u, \quad [4]$$

where "nm" is the number of minerals, and " fr_m " and " fr_u " are the volume fraction of mineral "m" in the rock and the volume fraction of nonreactive rock, respectively.

In our simulations the permeability changes associated with changes in porosity are calculated from the following simplified cubic law:

$$k = k_i \times \left(\frac{\phi}{\phi_i} \right)^3 \quad [5]$$

where k_i and ϕ_i are the initial permeability and porosity, respectively. Because of the complexity and diversity of the pore geometry of natural geologic media, a generally valid porosity-permeability relationship is not realistically attainable (Raffensperger, 1996), and different formulations may be preferable in some cases (Pape et al., 1999; Xu et al., 2004b).

Mass transport equations and chemical reaction equations are considered as two relatively independent subsystems, and they are solved separately in a sequential manner following an iterative procedure. Mass transport equations are written in terms of total dissolved component concentrations.

The advection contribution to the total mass of chemical species transported in liquid phase is given by the following relationship:

$$m_{adv}^j = \frac{\Delta t}{V_n} \times \sum_m A_{nm} \times u_{nm} \times C_{nm}^j \quad [6]$$

where m_{adv}^j is concentration of the advected basis species j , n and m label the reference and their adjacent grid blocks, respectively (m -th blocks are connected to every reference n -th block), Δt is the time step, V_n the volume of the n -th reference grid block, A_{nm} the interface area, u_{nm} the Darcy's velocity, and C_{nm}^j the concentration of the basis species.

Diffusion occurs only in the liquid phase and relevant parameters are as follows: specific diffusion coefficient (D_e) is a constant for all aqueous species set to 10^{-9} m²/sec (averaging the values reported by Oelkers and Helgeson (1988) for a large number of ionic species in aqueous solution), and tortuosity is calculated according to the Millington and Quirk (1961) equation:

$$\tau_0 \times \tau_\beta = \phi^{\frac{1}{3}} \times S_\beta^{\frac{10}{3}} \quad [7]$$

where $\tau_0 \times \tau_\beta$ is the tortuosity which includes a porous medium dependent factor τ_0 and a coefficient that depends on phase saturation S_β , $\tau_\beta = \tau_\beta(S_\beta)$ (Pruess et al., 1999).

The diffusion contribution to the total mass of chemical species transported in liquid phase is given by the following relationship:

$$m_{diff}^j = \frac{\Delta t}{V_n} \times \sum_m A_{nm} \times D_{nm} \times \left[\frac{C_m^j - C_n^j}{d_{nm}} \right] \quad [8]$$

where m_{diff}^j is concentration of the basis species j transported by diffusion, D_{nm} is the diffusion coefficient in the aqueous phase, $\left[\frac{C_m^j - C_n^j}{d_{nm}} \right]$ is the difference in concentration of the j-th basis species between the “m” and “n” adjacent blocks, divided by the internodal distance d_{nm} , and all other symbols are as in equation [6]. The conservation equations for diffusion are written here in terms of total concentrations because diffusion coefficients are assumed the same for all species in aqueous solution. Even if this assumption is not strictly true, it is

widely made in the implementation of multi purpose reactive-transport codes such as TOUGHREACT, because it simplifies the mathematical resolution of the reactive-transport problem (e.g. Steefel and Lasaga, 1994; Lichtner, 1985; Lasaga, 1979).

Both reservoir and caprock domains are modeled as porous media. Below, details are given for the different physical and geochemical initialization parameters used for these two rock domains.

3. Initial mineralogy

Reservoir formations mainly consist of sandstones with a significant component of carbonate (see Table 1; calcite and dolomite, about 16% by volume) and clay minerals (muscovite, chlorite, kaolinite, illite, Na-smectite, about 31% by volume). Bulk mass is represented by non-clay silicates like quartz, K-feldspar and albite (53% by volume on average).

The caprock is composed of carbonate-rich shales, made up of 33% by volume of calcite+dolomite and 47% by volume of silicate clay minerals, represented in order of decreasing abundance by muscovite, Na-smectite, chlorite, kaolinite and illite. Non-clay silicates are represented by quartz, which amounts to 20% by volume.

Sensitivity studies were carried out with respect to initial mineralogical compositions spanning the range shown in Table 1.

For the sake of simplicity, average compositions have been identified for both caprock and reservoir domains, and unless stated otherwise, these compositions have been considered in all the simulations presented in the following chapters for a “prototypical reference scenario” (hereinafter called PRS). These reference, average compositions are given in Table 1.

4. Initial aqueous solutions

Analytical data were available only for the aqueous solution of the reservoir. The available sample refers to a brackish water, of intermediate salinity between brines (up to 100 g/L Cl⁻) generally occurring at depth within the system and dilute, superficial waters (few ppm Cl⁻), possibly entering the reservoir in marginal and more heavily depressurized areas. This water (Table 2) has been assumed to be representative of the fluids present in the shallowest layer of the reservoir, located immediately below the caprock. Inspection of mineral saturation indices reveals that this analytical water is not completely equilibrated at 45°C with reservoir diagenetic minerals. Batch modelling calculations indicate that when this water is allowed to react with the primary mineralogy of the reservoir, a significant variation in the overall chemistry of the aqueous solution is predicted to occur, associated with almost negligible variations in the primary mineralogical assemblage. For instance, the code predicts the dissolution of albite, illite and calcite (with a maximum decrease of -13.5, -2.4 and -3.4 g mineral per liter of medium, respectively), and the precipitation of Na-smectite, K-feldspar, dolomite and muscovite (with a maximum increase of +10.5, +6.6, +3.7 and +1.0 g mineral per liter of medium, respectively) after 1000 years simulation. These variations are not significant in terms of modal abundances, because only albite (-1.3%) and Na-smectite

(+1.2%) show variations larger than 1% by volume, as that porosity remains almost fixed around the original value of 32.5%. Further simulations (not discussed here) indicate that the geochemical variations induced in the reservoir due to this initial small degree of thermodynamic disequilibrium between water and rock determine minor chemical perturbations in the caprock. The effects of these perturbations are almost negligible if compared with those related to the advancement of the pH-acid reactive front induced by CO₂ injection at depth (see simulations discussed below, and Figures 6A and 6B).

No analytical data exists for the caprock pore waters. The initial aqueous solution for the caprock (Table 2) has been generated through an iterative batch modeling procedure, starting from data on primary mineralogy (Table 1) and arbitrarily fixing total salinity at similar values as the underlying reservoir waters (about 1.5m NaCl).

Different initial trial solutions were utilized in order to obtain a reasonably stable water composition consistent with the local geochemical setting, i.e. an aqueous solution nearly saturated with respect to relevant primary caprock minerals listed in Table 1. The search for such a “best fitting water” has been carried out iteratively, following a trial and error procedure. The small degree of thermodynamic disequilibrium between the “reconstructed” pore water and the primary mineralogy causes only negligible geochemical variations in the caprock on the short to medium term, which is the objective of this study. After 1000 years simulation time, the maximum variations in volumetric abundance for illite, Na-smectite, muscovite, dolomite and calcite, are predicted at -1.1%, +0.6%, +0.5%, +0.08%, and -0.07%, respectively, and all the remaining mineral and chemical concentrations in the aqueous phase remained almost constant with time. These minor variations in the modal abundance of the relevant minerals cause a small variation in porosity of about +0.02%. More significant effects

are expected to occur only on the long term, e.g. after several thousand of years. More details on these procedures are given in Gherardi et al. (2005).

5. Thermodynamic and kinetic parameters

The mineralogy of the system is described in terms of 10 primary minerals, and 12 secondary minerals, as shown in Tables 1 and 3. The selected initial mineralogy reflects some conceptualization of the observed assemblage. This conceptualization is needed because the description of minerals is not always sufficiently specific to resolve the contribution of undifferentiated minerals like micas and clay minerals.

For example, in our database chlorite group minerals are represented by means of a single mineral which is marked “chlorite” ($\text{Mg}_{2.5}\text{Fe}_{2.5}\text{Al}_2\text{Si}_3\text{O}_{10}(\text{OH})_8$), and is intermediate in chemical composition with respect to Mg- and Fe-enriched end-members daphnite-14Å ($\text{Fe}_5\text{Al}_2\text{Si}_3\text{O}_{10}(\text{OH})_8$) and clinochlore-14Å ($\text{Mg}_5\text{Al}_2\text{Si}_3\text{O}_{10}(\text{OH})_8$). Illite group minerals are represented by a single mineral (“illite”), characterized by the following chemical formula $\text{K}_{0.6}\text{Mg}_{0.25}\text{Al}_{1.8}(\text{Al}_{0.5}\text{Si}_{3.5}\text{O}_{10})(\text{OH})_2$. Na- and Ca-smectite are assumed to have the following chemical formulas: $\text{Na}_{0.29}\text{Mg}_{0.26}\text{Al}_{1.77}\text{Si}_{3.97}\text{O}_{10}(\text{OH})_2$ and $\text{Ca}_{0.145}\text{Mg}_{0.26}\text{Al}_{1.77}\text{Si}_{3.97}\text{O}_{10}(\text{OH})_2$. The existence of possible solid solutions has not been taken into account.

Thermodynamic data for minerals, gases and aqueous species are mostly taken from the EQ3/6 V7.2b database of Wolery (1992). Some substitutions and changes have been incorporated to account for recent published revisions in thermodynamic properties of rock

forming minerals and aqueous species. Details on data sources and the list of chemical species for which thermodynamic parameters have been updated, are given in Xu et al. (2005).

Some of the most relevant kinetic parameters are summarized in Table 3. They are taken from Xu et al. (2004c), Xu et al. (2005), Palandri and Kharaka (2004), and references cited therein. Reactive surface area for each mineral is calculated from the specific reactive area and the quantity of each mineral, assuming that the reactive surface is proportional to mineral volume fraction, as detailed by Xu et al. (2004a). Due to the large natural variability and uncertainty in the measurement of specific reactive areas of minerals, no sensitivity analysis has been performed with respect to this parameter. Initial values have been set according to literature data, accounting for the larger intrinsic surface areas of clay minerals with respect to other minerals.

Sensitivity analyses have been performed for the kinetic rate laws, to evaluate how the numerical results were affected by the large uncertainty in the product of the reactive areas and the rate laws (see, among many others, Brantley, 2003; White 2003, and references cited therein). In particular, the precipitation and dissolution kinetic constants of calcite (which are the most important kinetic parameters in our simulations, see sections below) have been varied by ± 3 orders of magnitude (covering an overall range of 6 orders of magnitude) with respect to the reference value of Table 3. Such a variability accounts for almost the complete range of values reported in literature for this parameter (e.g. Morse and Arvidson, 2002, and references cited therein). Under the conditions specific for this study, the sensitivity simulations indicated that no relevant variations in the geochemical behavior of the system are predicted when the kinetic rates for carbonate and silicate minerals are let to vary within

geochemically reasonable range of values, as reported in the literature (e.g. White and Brantley, 1995, 2003; Brantley, 2003; White, 2003; and references cited therein). For this reason, this aspect will not be further discussed in the present paper.

6. Initial physical parameters

Simulations were carried out for isothermal conditions of 45 deg-C, and 105 bar total pressure, which corresponds to the values currently measured at the top of the reservoir. Variations in total pressure, which based on field data are expected to occur up to 150 bar after the beginning of CO₂ injection, do not affect the reliability of the numerical results. This is because the overall fluid dynamics (and reactivity) of the caprock-reservoir system, is controlled more by ΔP values at the interface between reservoir and caprock, than by the absolute value of total pressure in the two rock domains.

Physical data utilized in the simulations are summarized in Table 4. Due to the lack of reliable data for the caprock domain, capillary pressure and relative permeability parameters, and functional dependencies on pressure and phase saturations have been taken from the literature (Pruess et al., 1999; Xu et al., 2004a,c). In particular, capillary pressure behavior is described through the van Genuchten (1980) relationship, which likely overestimates gas-phase transfer from reservoir to caprock, because it does not provide a “gas entry-pressure” value.

Permeability, porosity and grain density have been set to average values reasonably representative of the system under study. Sensitivity analyses were performed with respect to caprock initial porosity (between 0.05 to 0.15) and permeability (0.001×10^{-15} to 0.1×10^{-15} m²). Both isotropic and non-isotropic spatial distributions of permeability have been tested for the caprock domain in the 2D models. Anisotropic conditions are modeled by setting k_z (vertical absolute permeability) = $0.1 \times k_x$ (horizontal absolute permeability).

7. Results and discussion

7.1. Sealed caprock: 1D simulations

One-dimensional diffusion through the caprock induced by aqueous solutes in the reservoir has been simulated by specifying a 1D vertical column of 1 m² cross-sectional area through the caprock. The volume of the reservoir block is 10 m³, while the caprock has been discretized using small grid spacing of the order of a few mm near the bottom, to better resolve chemical concentration gradients near the caprock boundary (Table 5).

The reservoir is initialized in two-phase conditions with initial CO₂ gas saturation $S_g = 0.3$, whereas the caprock is assumed to be fully liquid-saturated ($S_L = 1.0$). Sensitivity with respect to initial reservoir gas saturation has been explored, and simulations were done for initial reservoir gas saturations varying from 0.1 to 0.9. The duration of the simulations is 100 years.

Under the initial conditions outlined above, transport in the caprock occurs exclusively by diffusion when capillary effects are neglected in the two-phase reservoir. In contrast, when capillary effects are accounted for, the general behavior of the system is not purely diffusion-controlled, as capillary effects induce advective flows at the reservoir-caprock interface which overwhelm the diffusively-driven behavior. In particular, the first caprock block makes a transition to two-phase conditions because of advective removal of water from the first block of the caprock, due to capillary suction from the reservoir below.

The two different cases are discussed in some detail below.

7.1.1. Mixed diffusive-advective transport

This simulation considers effects of capillary pressure in the reservoir, which serves to draw down some water from the caprock, and causes gas to migrate upward.

Due to gas ingress into the caprock, the system under investigation is characterized by strong reactivity.

As a consequence, massive dissolution/precipitation reactions occur, and the porosity declines to near zero in the second element of the caprock after only 6.6 years (Figure 1).

The nodal point of this element is located at 2.5 mm from the interface with the reservoir. The graph of Figure 1 also shows that porosity is significantly enhanced in the first element of the caprock, whereas above the interface between the first and second element of the caprock a reversal of this pattern occurs, with a marked reduction in pore spaces in the second and, to a

lesser extent, in the third element of the caprock. The contrasting behavior between elements 1 and 2 of the caprock is strictly correlated with the propagation of the “free-gas front”. In fact, two-phase conditions develop only in the first element of the caprock ($S_g = 0.01$), where high P_{CO_2} conditions and low pH values in the aqueous solution are maintained. That increases the chemical reactivity of the system.

Porosity rapidly declines in the second block due to massive precipitation of calcite, induced by (1) aqueous Ca increasing in the first block, (2) diffusion of aqueous Ca into the second block, and (3) buffering of pH in the second block.

Based on pH values distribution, a kind of “geochemical divide” can be recognized within the column. Such bipartitioning of the system is almost instantaneous and occurs at the interface between the first and the second element of the caprock. According to this general picture, quite acidic conditions ($pH = 4.8$) develop at the beginning of the reaction within the reservoir and the first element of the caprock, whereas in the upper part of the column pH is buffered at some higher value, around 7.0.

The most important process controlling the chemical evolution of the system is the dissolution/precipitation of calcite. Calcite tends to dissolve within the reservoir and the first element of the caprock, whereas it precipitates in the upper part of the column, particularly in the second element of the caprock. This behavior is shown in Figure 2, where the changes in volume fraction (with respect to total medium) of calcite and porosity after 5 years simulation are shown for the reservoir and the first 100 cm of the caprock. By inspection of these

patterns, a clear inverse correlation between calcite precipitation/dissolution and porosity decrease/increase near the reservoir-caprock interface is recognized.

Dissolution of calcite in the reservoir and first element of the caprock is driven by acid pH conditions induced by high P_{CO_2} values. Calcite dissolution makes available further Ca_{TOT} and C_{TOT} (where the subscript "TOT" means here and hereinafter "total concentrations") to the aqueous solution. High P_{CO_2} values also imply high $CO_{2, aq}$ activities. Aqueous Ca and C diffuse into the caprock, as lower concentrations of these species are present in the upper part of the caprock. The concentration gradient between reservoir and first element of the caprock on the one hand, and the upper part of the caprock column on the other, is large and induces an upward, nearly constant flux of these (and other) species through the column (see Figure 3).

Diffusive flux of Ca_{TOT} and C_{TOT} leads to calcite precipitation and sealing of void spaces in the second element of the caprock, where fully liquid ($S_L = 1.0$) and near neutral ($pH \approx 7.0$) conditions still persist. This process is predominant over the competing proton diffusion process induced by acidification of the reservoir. In the idealized conditions of the proposed model, the mineralogical composition of the system acts as an effective buffer which impedes further propagation of the acid front created by high $P_{CO_2(g)}$ conditions in the reservoir. Sealing occurs rapidly due to very fast kinetics of calcite precipitation.

This overall behavior can be easily traced in terms of calcite saturation index. Data after 5 years simulation indicate that calcite is slightly undersaturated in the RES 1 and CAP 1 grid blocks, and slightly oversaturated in the second element of the caprock ($SI = +0.0012$). Such a small degree of oversaturation, provides the thermodynamic driving force which induces the

efficient calcite precipitation predicted by the code (3.3×10^{-6} , 3.0×10^{-6} and 9.2×10^{-7} mol/sec after 0.1, 1 and 5 years, respectively).

In agreement with different pH conditions developing along the column, the mineralogy evolves following quite different trends on the opposite sides of the one-to-two-phases interface. Precipitation/dissolution processes involving minerals other than calcite are not significant for the control of porosity during the first 10 years of simulation, but in some cases they play a significant role in terms of control of the chemical composition of the aqueous solution. The most relevant processes are those involving dolomite, illite, chlorite and Na-smectite.

Dolomite and illite tend to precipitate and dissolve, respectively, within both reservoir and caprock domains. In contrast, chlorite and Na-smectite show a more complicated and opposite behavior: during an initial transient phase of about 1 year, chlorite precipitates in elements 2 and 3 of the caprock (with calculation points at 2.5 and 8.5 mm from interface) and dissolves within the reservoir and first element of the caprock, whereas the opposite occurs for Na-smectite. After this time, a clear tendency towards a progressive dissolution and precipitation for chlorite and Na-smectite is predicted all over the caprock domain (Figure 4).

These reactions control most of the aqueous chemistry, and particularly Mg aqueous concentrations (Figure 5, box A), as this element is present in all these minerals. Among the major aqueous constituents, only Ca- and C-bearing species are not significantly affected (Figure 5, boxes B, E, F), because they are mainly controlled by dissolution and precipitation

reactions involving carbonate minerals. Dissolution of illite in the caprock makes available in solution also significant amounts of Fe (Figure 5, box G), which then diffuses through the caprock leading to precipitation of minor secondary ankerite and siderite throughout the system, reservoir included.

K amounts derived from dissolution of illite are partly fixed within the reservoir as muscovite and K-feldspar, and partly diffuse through the caprock where they mostly remain in aqueous solution (Figure 5, box C). The resulting pattern in the reservoir is of progressive K depletion.

Na concentrations change according to the chemical gradient present in the system, i.e. they tend to back-diffuse from caprock to reservoir (Figure 5, box D). This “reverse” chemical gradient is partly due to the slightly different initial Na concentrations in the two domains (more Na in the caprock), and in part is also enhanced by the dissolution of Na-smectite occurring in the caprock. Na-smectite and dawsonite precipitation in the reservoir only partially buffer Na concentrations, due to the relatively slow kinetics of these minerals (in particular Na-smectite), and due to the continuous supply of this ion deriving from the concomitant dissolution of albite. The net effect of all these processes is a smoothed increase in Na concentration within the reservoir.

Total silica (Figure 5, box H) and Al concentration patterns reflect the interplay of almost all of the process previously described, as both of these species are involved in the precipitation/dissolution reactions of all the silicates and Al-silicates taken into consideration in the simulation. In particular, $\text{SiO}_{2(\text{aq})\text{TOT}}$ concentrations increase by a factor greater than two in the reservoir, due to a net positive balance between source terms, represented by illite,

chlorite and albite dissolution, and sink terms, represented by quartz, kaolinite, K-feldspar, muscovite, Na- and Ca-smectite precipitation.

Al_{TOT} shows a complex pattern, characterized by an increase in the grid blocks where two-phase conditions develop (reservoir and first element of the caprock), due to a local predominance of Al-silicate dissolution over precipitation reactions, and an initial decrease in the adjacent elements of the caprock (CAP 2 and CAP 3), due to a reversal of this unbalanced condition.

The temporal evolution of the chemical composition of reservoir pore waters is shown in Figure 6.

7.1.2. Purely diffusion-controlled transport

In this simulation, capillary pressures in the reservoir are neglected. All elements of the caprock remain in fully liquid-saturated conditions and no advective flow occurs. Under these conditions the geochemical effects driven by diffusion in the aqueous phase can be easily investigated. Based on preliminary fluidodynamic simulations (not presented here), these conditions are expected to occur in some marginal areas of the field, not far from the anticline structures where bouyancy forces tend to concentrate the free gas phase. Here, the gas plume would not displace the pore waters, as that liquid saturation remains fixed at relatively high values (i.e. $S_L > 0.7$), and it would not penetrate into the overlying caprock. Under these conditions, the free gas phase behaves as a passive bystander which only buffers the pH of the reservoir aqueous solutions.

As no gas front advancement is observed, pH remains buffered at some near-neutral values (between 6.92 and 7.04, depending on time) also in the first element of the caprock, due to calcite precipitation. Calcite precipitation occurs almost instantaneously in the first element of the caprock (Figure 7, box A) with an increase of about 400 g/L medium in less than 1 year. Calcite initially slightly dissolves in the reservoir (up to -0.95 g/L medium after about 1 year), and then precipitates (+0.02 g/L medium in the time range between 1 and 5 years). Initial calcite dissolution in the reservoir makes available further Ca_{TOT} and C_{TOT} in aqueous solution, which diffuse into the caprock where lower initial concentrations occur. Due to the high initial difference in concentration between the reservoir and caprock domains, Ca supply from the reservoir remains almost constant in time until the pores clog (porosity declining to near-zero in the first element of the caprock after only 1 year. The efficient buffering of pH predicted in the caprock may be in part related to the formal treatment of the diffusive reactive chemical transport currently implemented in TOUGHREACT (Xu et al., 2004a), which does not account for the consistently higher diffusivity of the proton with respect to other concurrent ions, such as Ca^{+2} and HCO_3^- (for instance, a factor of about 9 is reported for H^+ to Ca^{+2} diffusivities in dilute aqueous solutions at 50°C; Oelkers and Helgeson, 1988). The assumption that diffusion coefficients are the same for all species in aqueous solution then likely lead to underestimate the propagation of the low-pH “dissolution-bearing” front, with respect to the counteracting “buffering front” of Ca^{+2} and HCO_3^- ions.

In contrast, when reservoir pore waters are prevented to interact with $\text{CO}_{2(\text{g})}$ injected at depth, the patterns for calcite and porosity result significantly smoothed (Figure 7, box B). Under these conditions, the chemical gradients between reservoir and caprock domains are in fact relatively small (e.g., pH is buffered at 6.71 and 6.88 in the reservoir and caprock,

respectively), and almost negligible calcite precipitation/dissolution occurs at the caprock-reservoir interface (up to -60 and -30 mg calcite per L of medium in the caprock and in the reservoir, respectively, after 10 years).

7.2.1. Medium-term and maximum risk scenario

On the basis of data from the previous simulations, a “maximum risk” scenario has been delineated in which caprock water-rock interactions occur in presence of a predominant CO₂-rich gas phase. To reproduce these conditions, two models have been defined in which CO₂ is allowed to directly penetrate into the caprock without any significant “chemical modulation”. This scenario should be reasonably representative of conditions occurring in the inner part of the CO₂ plume, near the injection wells, after the injected CO₂ has completely displaced the brines initially present in the reservoir. An outline of the two models is given below.

In the first group of simulations (“advection case”), a large, variably overpressurized reservoir almost completely filled with CO₂ ($S_g = 0.99$), is specified below the caprock column with the aim to force the gas to move upwards. At the same time, aqueous solution from the caprock is not allowed to move downwards into the reservoir, to avoid spurious advective flows through the column.

In the second group of simulations (“injection case”), CO₂ was directly injected into the bottom element of the caprock by means of an external source term, in a manner that completely excludes the reservoir domain from the simulation.

In the first model, the extent of reservoir overpressure is the critical parameter that determines the propagation velocity of the gas front; in the second model, this role is played by the CO₂ injection rate. As no reliable field data are currently available to constrain these parameters, a sensitivity analysis was performed. Reservoir overpressure has been varied in our simulations between +1 to +20 bar (the maximum overpressure expected in the reservoir due to CO₂ injection), and injection rates of (anhydrous, supercritical) CO₂ have been varied between 0.1 to 10 kg CO₂ per year per m².

Here, the results for the injection case are discussed in some detail, because under these conditions, the calculations allow to characterize the geochemical effects induced by CO₂ front advancement in the caprock, without any contribution from reservoir water molecular diffusion.

With respect to the previous 1D simulations, in this run the initial porosity (now set to 0.1) and the absolute permeability (now 10⁻¹⁷ m²) have been changed. In addition, in order to achieve a larger maximum simulation time (500 years), the grid spacing ($\Delta z_{\text{MIN}} = 0.1$ m) and the maximum length of the column ($z_{\text{MAX}} = 50.4$ m) have also been increased.

More details on grid discretization are given in Table 6.

The advancement of a CO₂-rich gas phase induces a significant pH lowering in the caprock (Figure 8, box A). After 50 years of simulation, pH is between 4.9 and 5 in the first 5 m of the caprock. After about 100 years, acidification reaches the fifteenth element of the caprock, at 10.90 m from the injection point. The low-pH front is at 15.90 m from the injection point after

200 years, and at 19.90 m, 22.40 m, 30.4 m and 36.4 m after 250, 300, 400 and 500 years, respectively. After about 150 years, the pH is stable at 4.8 - 4.9 in the first 12 m of the caprock.

A supercritical free gas phase develops in the first element of the caprock after only one year, whereas 3 and about 6.2 years are needed for free gas to evolve in the second and third element, respectively (Figure 8, box B). After 500 years the maximum gas saturation level is about 0.22 in first few meters of the caprock, and about 0.2 at 10.90 m from the injection point (ELE15).

After an initial slow increase due to the fast kinetics of calcite dissolution, porosity progressively decreases in the caprock due to the low-pH, high $\text{CO}_{2(\text{aq})}$ gas-driven front propagation, which induces some mineralogical modifications in the clay and carbonate mineral fractions (Figure 9). After 500 years the porosity decrease predicted by the code is less than -0.2% between 35 to 100 cm (ELE 2 to ELE15) from the injection point, and even less (-0.14%) in the first element of the caprock.

Similar results are obtained also when higher injection rates ($10 \text{ kg CO}_2 \text{ yr}^{-1}$) are applied for longer simulation times (1000 yrs). Under these conditions the system responds more rapidly, and porosity change is similar for the first 12 m from the injection point after 1000 years of simulation. The maximum porosity decrease is -0.0022 in the first grid block ELE 1 after 1000 yrs.

The mineralogical composition of the caprock changes only slightly in response to CO₂ injection. Inspection of major mineralogical transformations reveals that porosity behavior results from the interplay of different precipitation/dissolution reactions, which can be summarized as follows:

1) calcite progressively decreases, with a maximum overall variation between -4.6 (distal point at 10.90m) and -6.9 (first element, at 10 cm) g/L medium;

2) carbonate minerals such as dawsonite and ankerite tend to form in the caprock; their maximum changes are between +6.9 and +9.4 g/L medium after 500 years;

3) dolomite also steadily increases throughout the caprock, showing positive delta values of about +1.4 g/L medium after 500 years;

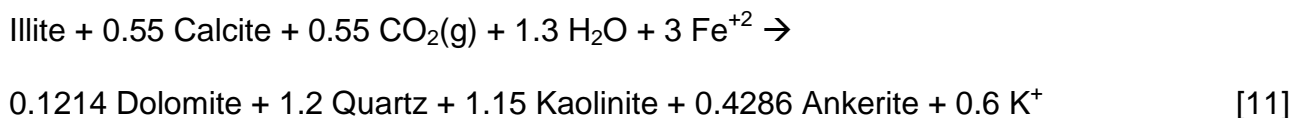
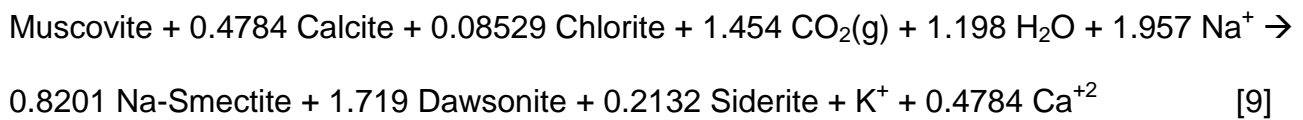
4) reactions involving Al-silicate minerals lead to the dissolution of chlorite and illite, and precipitation of Na-smectite; maximum concentration changes for these minerals are observed after 500 years, and correspond to about -8.2, -3.1 and +11.7 g/L medium, respectively;

5) muscovite has a more complex pattern, with an initial dissolution stage (up to -8.8 g/L medium after about 330 years), and a final precipitation stage which leads to the formation of about 0.5 g mineral per L medium between 330 and 500 years;

5) minor kaolinite precipitation (about 0.2 g/L medium after 500 years) is predicted;

6) finally, quartz shows a non-uniform behavior throughout the column; it tends to precipitate near the injection point, and to slightly dissolve at larger distances, due to initial not fully equilibrated conditions with respect to caprock “synthetic” pore waters (this effect is estimated in a maximum dissolution of less than 5 mg mineral per L medium after 500 years); CO₂-rich gas front arrival has the net effect to induce some minor quartz precipitation (up to a maximum of less than 15 mg/L medium after 500 years).

On the basis of the medium-term 1D simulation results, a chemical characterization of the reactive mechanisms induced by CO₂ penetration in the caprock is obtained. The following overall reactions, which account for the major concentration changes occurring in both the aqueous and solid phases, can be tentatively written:



Even if not stoichiometrically representative of processes effectively occurring within the caprock (stoichiometric coefficients have been included in eqs. [9] to [11] only to honour mass

balance constraints), these equations have the main advantage to completely represent the main mineralogical transformations. They explain the progressive increase of Ca_{TOT} and K_{TOT} aqueous concentrations observed at the end of the simulation, and also the eventual decline of the maximum Fe_{TOT} amounts originally derived from chlorite and illite dissolution.

Accordingly, such reactions are proposed here to synthesize in a compact form the complex multicomponent and multiphase reactive processes effectively occurring in the caprock due to $CO_2(g)$ injection. Their validity is supported by inspection of thermodynamic concentrations, which indicate the energetic feasibility of the processes where high P_{CO_2} -values occur.

7.3. Fractured caprock: 2D simulations

7.3.1. Medium-term and maximum risk scenario

As in the case of 1D simulations, a maximum risk scenario for the fractured caprock model is obtained by maximizing the participation of gaseous CO_2 in water-rock interactions. This has been accomplished by applying the “advection” and “injection” models already described in section 7.2.1.

In particular, by setting appropriate initial and boundary pressure conditions (see below), the CO_2 initially stored in the reservoir is forced to first invade the fracture, and to subsequently enter the rock matrix, whereas fluids from the matrix are allowed to freely discharge away from the fracture. This model conceptualizes the behavior of a semi-infinite matrix layer which extends perpendicularly to the fracture axis.

In the case of the advection model, the dynamics of CO₂-rich fluids has been represented by applying (i) a constant overpressure at the fracture bottom (+2 bar for the “reference case”), and (ii) a constant underpressure ($\Delta P = -0.1$ bar, calculated node-by-node with respect to numerical values obtained at the end of an initial gravity equilibration) at the rightmost boundary of the matrix domain. In the injection model the amount of CO_{2(g)} entering the fracture domain is controlled by means of a constant-rate source term set in the lowermost element of the fracture domain, which in the “reference case” causes CO_{2(g)} to penetrate into the caprock with a flux rate of 1 kg per year per m². The same underpressure condition as in the advection model is used at the lateral boundary of the matrix domain.

Because larger simulation times were desired ($\text{time}_{\text{MAX}} = 500$ years), a coarser grid has been utilized ($\Delta z_{\text{MIN}} = 5$ cm) to reduce the computational work of the simulation. The maximum lateral and vertical extension of the caprock domain now reaches 12.58 m and 20.55 m, respectively. More details on grid specifications and system geometry are given in Figure 10.

The main driving forces controlling fluid displacement in our system can be recast in terms of pressure gradients, and some understanding of flow dynamics within the caprock can be obtained through the inspection of pressure and capillary pressure profiles (Figure 11). In particular, we can observe that: (i) the gas flows primarily along the fracture (with a maximum velocity of about 8×10^{-5} m/sec after 500 years), and enters the matrix only slowly (up to about 10^{-11} m/sec after 500 years), following a direction perpendicular to the fracture axis; (ii) liquid dynamics is characterized by a preferential upward displacement along both the fracture domain and the adjacent matrix columns (with high porosity and permeability values). This has the ultimate effect of inducing slow convection in the inner part of the matrix (Figure

12), and promoting some mixing between different waters. As deduced from these diagrams, mass transfer occurs in the matrix under control of the following concomitant mechanisms: gas advection, molecular diffusion in aqueous phase, and liquid advection.

The advancement of the CO₂-rich gas front in the caprock is traced by the presence, after 500 years simulation, of gas saturation values > 0 at more than 1 m from fracture axis (Figure 13). At this simulation time the gas front has advanced about 1.75 m into the matrix near the bottom of the domain, and about 1.25 m in the middle and at the top of domain. At the same simulation time, the pH pattern roughly follows the gas saturation pattern, only differing from it for a more uniform advancement of the pH-acid front along the direction perpendicular to the fracture axis. pH contour lines are almost exactly aligned in a vertical direction (Figure 13), and minor deviations are shown for the lower values only, as e.g. for the pH = 5 isoactivity line which is at 0.8 and 1.2 m from fracture axis in the upper and lower part of the domain, respectively.

Porosity and calcite variations inversely correlate all throughout the caprock domain (Figure 14), indicating that dissolution/precipitation mechanisms involving this mineral exert the dominant control on porosity enhancement/reduction. This is in agreement with the intrinsic fast kinetics of calcite.

A major difference with respect to previous simulations is the large increase in porosity predicted for the fracture domain. This porosity enhancement reaches a maximum of about +0.14 (expressed as volume fraction normalized to total volume of porous medium) when the advection model is applied, which means a maximum total porosity of about 0.64 in the

fracture (the initial porosity was 0.50). Large variations also occur in the adjacent matrix columns, as shown by delta values of +0.10 and +0.06 at 0.05 and 0.1 m from the fracture axis, respectively. In the case of the injection model even stronger effects are predicted, with a maximum increase in porosity of about +0.19 (from the initial 0.5 to the final 0.69, after 500 years simulation) in the lower part of the fracture domain, near the interface with the reservoir.

This overall behavior reflects the fact that calcite dissolution due to CO₂-driven acidification is now very effective, independent from which model (“advection” vs. “injection”) is applied. In fact, under the conditions of the fractured caprock model, pH is kept low wherever gaseous CO₂ is able to flow, due to the fact that the competing (with respect to calcite thermodynamic stability) supply of Ca and C from reservoir is minimized.

The mineralogical transformations involving minerals other than calcite are quantitatively negligible also after 500 years of simulation. The most relevant changes correspond to muscovite dissolution (up to -0.02 porous medium volume fraction, at the top of the matrix, near fracture domain; Figure 15, box A), and Na-smectite precipitation (up to +0.016 porous medium volume fraction, in the same part of matrix domain; Figure 15, box B).

Overall trends (after 500 years of simulation) for the remaining minerals are as follows:

1) chlorite and illite steadily dissolve (Figure 15, boxes C and D), and the maximum decrease in volume fraction occurs along a vertical direction, in the matrix columns adjacent to fracture domain; maximum delta values are about -0.003 and -0.001 for chlorite and illite, respectively;

2) carbonate minerals like ankerite, dolomite and dawsonite (Figure 16, boxes A and B) tend to precipitate in the same zones where clay minerals like muscovite, chlorite and illite dissolve; dawsonite shows the maximum increase (about +0.015), followed by ankerite (up to about +0.003) and dolomite (up to about +0.0005);

3) kaolinite and quartz (Figure 16, boxes C and D) have the same complex pattern, characterized by precipitation in the zones where lowest pH conditions develop, i.e. near the fracture, and dissolution in the inner part of the matrix; delta values are very low and span the range $+10^{-4}$ to -5×10^{-5} , and $+1.6 \times 10^{-6}$ to -10^{-5} for kaolinite and quartz, respectively.

Coupled with information on spatial distribution of aqueous components concentration, these data reveal that long term $\text{CO}_{2(g)}$ advection through the fracture induces a consistent lowering in pH, and gives rise to the following changes in the aqueous chemical composition of the caprock:

1) a large increase in C_{TOT} concentration, due to gas dissolution;

2) an appreciable increase in Fe_{TOT} , Mg_{TOT} , Al_{TOT} and $\text{SiO}_2(\text{aq})_{\text{TOT}}$ concentrations, due to Al-silicate dissolution (chlorite, illite and muscovite) and diffusion induced by fluids migrating in the fracture;

3) a decrease of Na_{TOT} concentration prevalently driven by molecular diffusion as a consequence of the fact that fluids in the fracture are Na-depleted with respect to fluids of the matrix domain.

The behavior of the fracture domain is critical for the evaluation of the sealing efficiency of the caprock. The code predicts that significant changes in the mineralogical facies of the solid fraction could occur after 500 years of simulation time in this part of the system.

With reference to the advection case, two major zones can be recognized at this time: the lower part of the column (up to about 5.55 m from reservoir interface) is characterized by the presence of variable concentrations of calcite (3.7 to 27.2% near the reservoir interface) and relatively lower porosities (between 50.8 to 62.8%); the upper part of the fracture domain (7 to 19.55 m from reservoir interface) is characterized by higher porosity (around 64.1%), lack of calcite, and higher concentrations of all other minerals.

Apart from massive calcite dissolution, major transformations in the upper part of the column involve Na-smectite (now representing 21.6 to 22.2% of the solid fraction), kaolinite (about 7.2%), dawsonite (less than 0.1%), siderite (less than 0.1%), dolomite (5.1%) and quartz (28.5 to 28.6%) precipitation, and muscovite (25.8 to 26.2%), chlorite (about 8.4%) and illite (about 2.8%) dissolution.

In Table 7 a summary of the average composition for the upper (the reference value is for the nodal block at 18.55 m from reservoir interface) and lower part of the fracture (reference value calculated at 0.5 m from reservoir interface) is given, together with the initial reference value of the caprock.

Inspection of spatial variation of chemical parameters further confirms that liquid advection and aqueous molecular diffusion from the reservoir (advection model) induce an increase in Ca_{TOT} and calcite saturation index within the fracture domain. This in turn, allows calcite to precipitate near the caprock-reservoir interface, when appropriate C_{TOT} concentrations and pH values occur, as previously shown for 1D simulations.

Far from the caprock-reservoir interface, Ca_{TOT} concentrations fall below some critical value allowing calcite to become undersaturated, and then to dissolve up to complete disappearance.

C_{TOT} concentrations are higher and spatially more homogeneous than Ca_{TOT} concentrations all along the fracture, suggesting that the spatial variations of Ca_{TOT} concentration is the limiting factor governing the overall geochemical behavior of the domain.

Water-rock interactions occur because non-zero liquid saturation values persist all throughout the fracture domain, in spite of the massive ingress of $CO_{2(g)}$ from the reservoir.

When higher initial pressures are specified in the reservoir, fluids are allowed to flow faster through the fracture. Under these conditions, chemical gradients between reservoir and caprock domains are smaller over a larger part of the fracture domain.

The presence of a such a “flow-controlled reactive regime” allows minerals that are kinetically and thermodynamically favored, such as calcite and dolomite, to precipitate more efficiently than before and, in the case of calcite, to start to dissolve at greater distances from reservoir interface (calcite is near saturation for the first 10 m of the fracture from reservoir interface).

At the same time, the onset of chlorite, kaolinite and illite precipitation is retarded (now at about 12 m), whereas the volume fraction of Na-smectite does not increase appreciably, according to the intrinsically slow kinetics of all these minerals. Also the porosity profile is

affected by the increased flow velocity: this effect is manifested in terms of spatial displacement of the maximum porosity value, which now occurs at about 12 m from reservoir interface, but not in terms of porosity enhancement, as the maximum porosity value remains near 0.64.

When the injection model is applied, a larger enhancement of the original porosity is predicted (Table 7). This behavior reflects the fact that the reservoir water is no more the mediator for the interactions between the migrating gas and host lithology of the caprock. Under these conditions, a more effective lowering of pH (Figure 17), and a massive dissolution of primary carbonate minerals (calcite and dolomite completely disappear) are calculated all along the fracture domain. The precipitation of appreciable amounts of secondary dawsonite (up to 6.1% of solid volume fraction) is also predicted at the top of the matrix, due to complex mixing relationships between C-rich fluids flowing through the fracture and aqueous solutions (bringing Na and Al) coming from the caprock matrix domain.

8. Conclusions

Models presented in this report are an idealization of the physical and chemical processes expected to occur in the caprock, as a consequence of CO₂ geological disposal in an on-shore, depleted gas field. Such models describe overall changes under specific assumed physical and chemical conditions which cannot be fully representative of the complexity of the system under study. Predictions of future scenarios cannot be considered “exact” at this

stage, and their accuracy would be greatly improved by the availability of more detailed site-specific physical and chemical data.

Major uncertainties are related to a lack of both laboratory and/or field data, and general information on the scatter of physico-chemical parameters in space. Numerical results are also affected by limitations of current reactive chemical transport simulators to reproduce the complex interplay of physical, hydrological and geochemical processes likely occurring in real systems. In this study, all these uncertainties have been handled through simplification of conceptual and geometric models, and by carrying out a sensitivity analysis on relevant geochemical features.

Future work could improve on these simplifications by (i) considering more realistic hydraulic conditions for the transport of gas and liquid phases between reservoir and caprock; (ii) representing gas invasion into the caprock with consideration of the wettability behavior of CO₂-brine mixtures, and relative permeability and capillary entry pressure effects in the caprock; (iii) considering variations in the composition of the initial aqueous solutions due to chemical heterogeneity of reservoir and caprock; (iv) considering species-dependent variations in the aqueous phase diffusion coefficients when simulations of diffusive-controlled reactive transport are performed.

Despite the simplifications and approximations used in our models, numerical simulations shed light on general geochemical trends that are important for mineralogical changes and sealing efficiency of the caprock in the presence of a CO₂-rich advancing fluid front.

Major conclusions are as follows.

1) Under the conditions investigated in this study, dissolution reactions may reduce the sealing efficiency of caprock formations when physical discontinuities occur, which would allow CO₂-rich fluids to advect upwards into the caprock. In contrast, molecular diffusion in the aqueous phase tends to induce reductions of porosity. In both cases, the overall geochemical behavior is controlled by dissolution/precipitation reactions involving calcite.

2) The overall geochemical behavior of the caprock domain is explained in terms of the following mechanisms. Liquid advection and aqueous molecular diffusion from the reservoir tend to increase Ca_{TOT} and HCO_{3,TOT} concentrations and calcite saturation index in the caprock. This induces calcite precipitation in the caprock when appropriate pH values occur, i.e., when the competing effect of pH lowering associated with the advancement of the CO₂-rich front is overwhelmed by increases in Ca_{TOT} and HCO_{3,TOT} concentrations. The main effect of gas advection is to increase CO₂ partial pressure and lower pH values, which will make calcite less thermodynamically stable in the caprock. The interplay between [Ca⁺²], [HCO₃⁻] and [H⁺] thus controls calcite dissolution/precipitation behavior in the caprock domain. This overall behavior predicted by the code can be rationalized in terms of competition between surface reactions and diffusive-advective transport of reactive species. The very fast kinetics of reactions involving calcite under low pH conditions is the constraint which allows this competition to exist.

3) The presence of a CO₂-rich gas phase has a strong influence on hydrogeochemical evolution of the caprock. Under conditions of predominantly advective transport, such as expected for a fractured caprock (2D models), CO₂(g) penetrates through the caprock and induces some enhancement in porosity and permeability. When transport of chemicals

primarily occurs by molecular diffusion in the liquid phase, as is expected for unfractured caprock (1D models), CO₂-leakage becomes self-limiting, and pores become clogged after a very short time.

4) The dominant role played by calcite overwhelms the effects of other mineralogical changes involving precipitation/dissolution of Al-silicate minerals. Even if not significant in terms of overall mass transfer, other mineral transformations induced by the advancement of the CO₂-induced acidic front in the caprock include clay dissolution (illite, chlorite and muscovite) and precipitation reactions (Na-smectite). Other effects include the formation of new minerals such as dawsonite, siderite, and ankerite. These results are in agreement with recent theoretical findings (e.g. Palandri and Kharaka, 2005), which demonstrated that ferric iron in sediments may act as a trap for CO₂, together with divalent metals such as Ca and/or Mg which are likely present in the rock matrix.

Acknowledgements

This work greatly benefited from the Editorial assistance of David Rickard, and criticisms from two anonymous reviewers. The authors also appreciate reviews of the manuscript and the suggestion of improvements by Guoxiang Zhang (LBNL), Alfredo Battistelli (SnamProgetti SpA) and Giovanni Gianelli (IGG-CNR). This work was supported by the Director, Office of Science, Office of Basic Energy Sciences of the U.S. Department of Energy under Contract No. DE-AC02-05CH11231, and by the Consiglio Nazionale delle Ricerche, Italy, under the SnamProgetti SpA contract No. 3000005218, in the framework of the ENI SpA “GreenHouse Gases” R&D project. Support by Stogit, EniTecnologie and ENI E&P Division is warmly acknowledged.

References

- Bachu, S., Gunter, W.D., Perkins, E.H., 1994. Aquifer disposal of CO₂. Hydrodynamic and mineral trapping. *Energy Conversion and Management* 35, 269–279.
- Brantley, S.L., 2003. Reaction Kinetics of primary rock-forming minerals under ambient conditions. In: *Treatise in Geochemistry* (Holland, H.D, Turekian, K.K., Eds), Volume 5, Surface and Ground Water, Weathering, and Soils, 73-117.
- Calabrese, M., Masserano, F., Blunt, M.J., 2005. Simulation of physico-chemical processes during carbon dioxide sequestration in geological structures. SPE 95820, Proceedings of the 2005 SPE Annual Technical Conference and Exhibition, Dallas, Texas, USA, 9-12 October 2005.
- Ennis-King, J., Paterson, L., 2000. Reservoir engineering issues in the geological disposal of carbon dioxide. In: Williams, D.J., Durie, R.A., McMullan, P., Paulson, C.A.J., Smith, A.Y. (Eds.), 5th International Conference on Greenhouse Gas Control Technologies, Cairns, Australia, pp. 290–295.
- Gaus, I., Azaroual, M., Czernichowski-Lauriol, I., 2005. Reactive Transport Modelling of the Impact of CO₂ Injection on the Clayey Cap Rock at Sleipner (North Sea). *Chemical Geology* 217, 319–337.
- Gherardi, F., Xu, T., Pruess, K., 2005. Exploratory simulation studies of caprock alteration induced by storage of CO₂ in depleted gas reservoirs. Lawrence Berkeley National Laboratory Report LBNL-59130, Berkeley, California.
- Gunter, W.D., Perkins, E.H., Hutcheon, I, 2000. Aquifer disposal of acid gases: modelling of water-rock reactions for trapping of acid wastes. *Applied Geochemistry* 15, 1085–1095.
- Helgeson, H.C., Kirkham, D.H., Flowers, D.C., 1981. Theoretical prediction of the thermodynamic behavior of aqueous electrolytes at high pressures and temperatures: IV Calculation of activity coefficients, osmotic coefficients, and apparent molal and standard and relative partial molal properties to 600 C and 5 kb. *American Journal of Science* 281, 1249–1516.
- Haszeldine, R.S., Quinn, O., England, G., Wilkinson, M., Shipton, Z.K., Evans, J.P., Heath, J., Crossey, L., Ballentine, C.J., Graham, C.M., 2005. Natural geochemical analogues for carbon dioxide storage in deep geological porous reservoirs, a United Kingdom perspective. *Oil & Gas Science and Technology* 60, 33-49.
- Hildebrand, A., Schlömer, S., Krooss, B.M., Littke, R., 2004. Gas breakthrough experiments on pelitic rocks: comparative study with N₂, CO₂ and CH₄. *Geofluids* 4, 61-80.
- Hitchon, B., 1996. Aquifer disposal of Carbon Dioxide. Hydrodynamic and Mineral Trapping – Proof of concept. In Geoscience Publishing Ltd., Sherwood Park, Alberta, Canada.
- Kaszuba, J.P., Janecky, D.R., Snow, M.G., 2003. Carbon dioxide reaction processes in a model brine aquifer at 200°C and 200 bars: implications for geologic sequestration of carbon. *Applied Geochemistry* 18, 1065– 1080.
- Kaszuba, J.P., Janecky, D.R., Snow, M.G., 2005. Experimental evaluation of mixed fluid reactions between supercritical carbon dioxide and NaCl brine: Relevance to the integrity of a geologic carbon repository. *Chemical Geology* 217, 277–293.

- Knauss, K.G., Johnson, J.W., Steefel, C.I., 2005. Evaluation of the impact of CO₂, co-contaminant gas, aqueous fluid and reservoir rock interactions on the geologic sequestration of CO₂. *Chemical Geology* 217, 339–350.
- Lasaga, A.C., 1979. The treatment of multi-component diffusion and ion pairs in diagenetic fluxes. *American Journal of Science* 279, 324-346.
- Lasaga, A.C., 1984. Chemical kinetics of water-rock interactions. *Journal of Geophysical Research* 89, 4009–4025.
- Li, Z., Dong, M., Li, S., Huang, S., 2006. CO₂ sequestration in depleted oil and gas reservoirs – caprock characterization and storage capacity. *Energy Conversion and Management* 47, 1372-1382.
- Lichtner, P., 1985. Continuum model for simultaneous chemical reaction and mass transport in hydrothermal systems. *Geochimica et Cosmochimica Acta* 49, 779-800.
- Lindeberg, E., 1997. Escape of CO₂ from aquifers. *Energy Conversion and Management* 38, S235–S240.
- Marschall, P., Horseman, S., Gimmi, T., 2005. Characterisation of gas transport properties of the Opalinus Clay, a potential host rock formation for radioactive waste disposal. *Oil & Gas Science and Technology* 60, 121-139.
- May, F., 2005. Alteration of wall rocks by CO₂-rich water ascending in fault zones: natural analogues for reactions induced by CO₂ migrating along faults in siliciclastic reservoir and cap rocks. *Oil & Gas Science and Technology* 60, 19-32.
- Millington, R.J., Quirk, J.P., 1961. Permeability of Porous Solids. *Transactions of the Faraday Society* 57, 1200–1207.
- Moore, J., Adams, M., Allis, R., Lutz, S., Rauzi, S., 2005. Mineralogical and geochemical consequences of the long-term presence of CO₂ in natural reservoirs: an example from the Springerville–St. Johns Field, Arizona, and New Mexico, U.S.A. *Chemical Geology* 217, 365–385
- Morse, J.W., Arvidson, R.S. (2002). The dissolution kinetics of major sedimentary carbonate minerals. *Earth-Science Reviews* 58, 51-84.
- Narasimhan, T.N., Whitherspoon, P.A., 1976. An integrated Finite Difference Method for Analyzing Fluid Flow in Deformable Porous Media. *Water Resources Research* 12, 57–64.
- Oelkers, E.H., Helgeson, H.C., 1988. Calculation of the thermodynamic and transport properties of aqueous species at high pressures and temperatures: Aqueous tracer diffusion coefficients of ions to 1000°C and 5 kb. *Geochimica et Cosmochimica Acta* 52, 63-85.
- Palandri, J.L., Kharaka, Y.K., 2004. A compilation of rate parameters of water-mineral interaction kinetics for application to geochemical modeling. US Geological Survey Open File Report 2004-1068, 64 pp..
- Palandri, J.L., Kharaka, Y.K., 2005. Ferric Iron-bearing Sediments as a Mineral Trap for CO₂ Sequestration: Iron Reduction Using Sulfur-bearing Waste Gas. *Chemical Geology* 217, 351–364.

- Pape, H., Clauser, C., Iffland, J., 1999. Permeability prediction based on fractal pore-space geometry. *Geophysics* 64, 1447 - 1460.
- Pruess, K., 1991. TOUGH2: A general-purpose numerical simulator for multiphase fluid and heat flow. Lawrence Berkeley National Laboratory Report LBL-29400, Berkeley, California.
- Pruess, K., Garcia, J., 2002. Multiphase flow dynamics during CO₂ disposal into saline aquifers. *Environmental Geology* 42, 282–295.
- Pruess, K., Oldenburg, C., Moridis, G., 1999. TOUGH2 User's guide, Version 2.0. Lawrence Berkeley National Laboratory Report LBNL-43134, Berkeley, California.
- Raffensperger, J.P., 1996. Numerical simulation of sedimentary basin-scale hydrochemical processes, In *Advances in Porous Media*, Corapcioglu, Y.C., (ed), Amsterdam, The Netherlands, Elsevier Science, 440 pp.
- Reed, M.H., 1982. Calculation of multicomponent chemical equilibria and reaction processes in systems involving minerals, gases and an aqueous phase. *Geochimica et Cosmochimica Acta* 46, 513-528.
- Rutqvist, J., Tsang, C., 2002. A study of caprock hydromechanical changes associated with CO₂-injection into a brine formation. *Environmental Geology* 42, 296–305.
- Spycher, N., Reed, M.H., 1988. Fugacity coefficients of H₂, CO₂, CH₄, H₂O and of H₂O-CO₂-CH₄ mixtures: A virial equation treatment for moderate pressures and temperatures applicable to calculations of hydrothermal boiling. *Geochimica et Cosmochimica Acta* 52, 739–749.
- Tanger, J.C., Helgeson, H.C., 1988. Calculation of the thermodynamic and transport properties of aqueous species at high pressure and temperatures: Revised equations of state for the standard partial molal properties of ions and electrolytes. *American Journal of Science* 288, 19–98.
- van Genuchten, M.T., 1980. A closed-form equation for predicting the hydraulic conductivity of unsaturated soils. *Soil Science Society of America Journal* 44, 892-898.
- Weir, G.J., White, S.P., Kissling, W.M., 1996a. Reservoir storage and containment of greenhouse gases. *Transport in Porous Media* 23, 37–60.
- Weir, G.J., White, S.P., Kissling, W.M., 1996b. Reservoir storage and containment of greenhouse gases. II. Vapour-entry pressures. *Transport in Porous Media* 23, 61–82.
- White, A.F., 2003. Natural weathering rates of silicate minerals. In: *Treatise in Geochemistry* (Holland, H.D, Turekian, K.K., Eds), Volume 5, Surface and Ground Water, Weathering, and Soils, 133-168.
- White, A.F., Brantley, S.L. (Eds.), 1995. *Chemical Weathering Rates of Silicate Minerals*. Reviews in Mineralogy, vol. 31. Mineralogical Society of America., Washington, D.C. 584 pp.
- White, A.F., Brantley, S.L., 2003. The effect of time on the weathering of silicate minerals: why do weathering rates differ in the laboratory and field?. *Chemical Geology* 202, 479-506.
- White, S.P., Allis, R.G., Moore, J., Chidsey, T., Morgan, C., Gwynn, W., Adams, M., 2005. Simulation of reactive transport of injected CO₂ on the Colorado Plateau, Utah, USA. *Chemical Geology* 217, 387–405.

- Wolery, T.J., 1992. EQ3/6: Software package for geochemical modeling of aqueous systems: Package overview and installation guide (version 7.2). Lawrence Livermore National Laboratory Report UCRL-MA-10662 PT I, Livermore, California.
- Xu, T., Sonnenthal, E., Spycher, N., Pruess, K., 2004a. TOUGHREACT User's Guide: A simulation program for non-isothermal multiphase reactive geochemical transport in variably saturated geologic media. Lawrence Berkeley National Laboratory Report LBNL-55460, Berkeley, California.
- Xu, T., Ontoy, Y., Molling, P., Spycher, N., Parini, M., Pruess, K., 2004b. Reactive Transport Modeling of Injection Well Scaling and Acidizing at Tiwi Field, Philippines. *Geothermics* 33, 477-491.
- Xu, T., Apps, J.A., Pruess, K., 2004c. Numerical simulation of CO₂ disposal by mineral trapping in deep aquifers. *Applied Geochemistry* 19, 917-936.
- Xu, T., Apps, J.A., Pruess, K., 2005. Mineral Sequestration of Carbon Dioxide in a Sandstone-Shale System. *Chemical Geology* 217, 295-318.
- Xu, T., Pruess, K., 1998. Coupled modeling of non-isothermal multiphase flow, solute transport and reactive chemistry in porous and fractured media: 1. Model development and validation. Lawrence Berkeley National Laboratory Report LBNL-42050, Berkeley, California.
- Xu, T., Pruess, K., 2001. Modeling multiphase flow and reactive geochemical in variably saturated fractured rocks: 1. Methodology. *American Journal of Science* 301, 16-33.
- Yeh, G.T., Tripathi, V.S., 1991. A model for simulating transport of reactive multispecies components: model development and demonstration. *Water Resources Research* 27, 3075-3094.

FIGURE CAPTIONS

Figure 1 – Evolution of porosity vs. time for selected grid blocks (1D, mixed diffusive-advective transport model; detail of first 10 years simulation; simulation time = 100 yrs). Sealing in the second element of the caprock occurs after 6.6 years.

Figure 2 – Change in calcite volume fraction and porosity in the reservoir and along the column (detail of first 100 cm) after 5 years simulation (1D, mixed diffusive-advective transport model).

Figure 3 – Change in C_{aTOT} and C_{TOT} aqueous concentration and calcite saturation index in the reservoir and along the column (detail of first 100 cm) after 5 years simulation (1D, mixed diffusive-advective transport model). Vertical patterns for pH and selected individual C species ($CO_{2(aq)}$, HCO_3^- , CO_3^{2-}) are also shown.

Figure 4 – Spatial (detail of first 50 cm of the caprock column, calculated from reservoir interface) and temporal (10 years simulation time) variation of chlorite and Na-smectite abundance in the caprock (delta g-mineral per L of medium).

Figure 5 – Spatial (detail of first 40 to 100 cm of the caprock column, calculated from reservoir interface) and temporal (10 years simulation time) variation of the chemical composition of pore waters in the caprock domain (1D simulation, reservoir $S_L=0.7$; mixed advective-diffusive transport model).

Figure 6 – Temporal variation of the chemical composition of pore waters in the reservoir (1D simulation, reservoir $S_L=0.7$; mixed advective-diffusive model).

Figure 7 – Temporal evolution of calcite abundances and porosity in selected caprock grid blocks and in the reservoir (1D simulation, purely diffusion-controlled transport model); box A: a CO_2 -rich gas phase ($S_L = 0.7$), and acidic pore waters are present in the reservoir; all parameters (apart from calcite in the reservoir) show a plateau after about 1 year, in agreement with the almost complete clogging predicted for the first element of the caprock; box B: no gas ($S_L = 0.7$), and near pH-neutral pore waters in the reservoir; smoothed patterns are predicted by the code under these conditions).

Figure 8 – pH (box A) and gas saturation (S_g , box B) patterns vs. time for selected grid blocks in the caprock (1D injection model, 500 years simulation).

Figure 9 – Spatial and temporal variation of selected geochemical parameters (box A: porosity; box B: $CO_{2(aq)}$ concentration, in mol/kg H_2O ; box C: calcite volume fraction; box D: Na-smectite volume fraction) along a vertical caprock column of 20 m, during a simulation time of 500 years (1D simulation, CO_2 -injection model).

Figure 10 – Vertical 2D section model for CO_2 leakage into a fractured caprock (500 years simulation). Details on porosity and permeability distribution are also given.

Figure 11 – Contour plots showing capillary pressure and absolute pressure (in Pa) distribution after 500 years simulation in the caprock domain (2D advection model; initial reservoir gas saturation, $S_g = 0.99$).

Figure 12– Contour plots showing liquid and gas darcian velocity fields (m/sec) after 500 years simulation in the caprock domain (2D advection model; initial reservoir gas saturation, $S_g = 0.99$).

Figure 13 – Contour plots showing gas saturation and pH spatial distribution after 500 years simulation in the caprock domain (2D advection model; initial reservoir gas saturation, $S_g = 0.99$).

Figure 14 – Contour plots showing porosity and calcite volume fraction change after 500 years simulation (2D advection model; initial reservoir gas saturation, $S_g = 0.99$).

Figure 15 – Contour plots showing muscovite (box A), Na-smectite (box B), chlorite (box C) and illite (box D) volume fraction change after 500 years simulation (2D advection model; initial reservoir gas saturation, $S_g = 0.99$).

Figure 16 – Contour plots showing ankerite (box A), dawsonite (box B), kaolinite (box C) and quartz (box D) volume fraction change after 500 years simulation (2D advection model; initial reservoir gas saturation, $S_g = 0.99$).

Figure 17 – Surface diagram showing spatial and temporal changes in pH within the fracture domain during 500 years simulation (2D injection model).

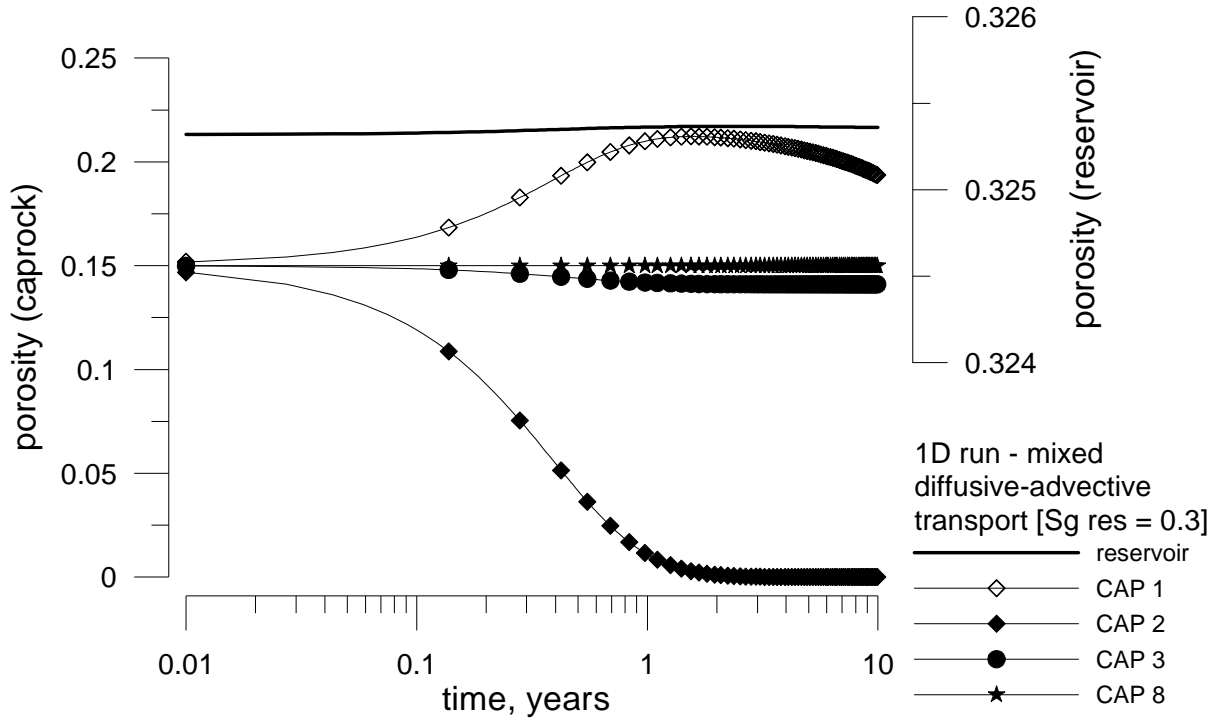


FIGURE 1

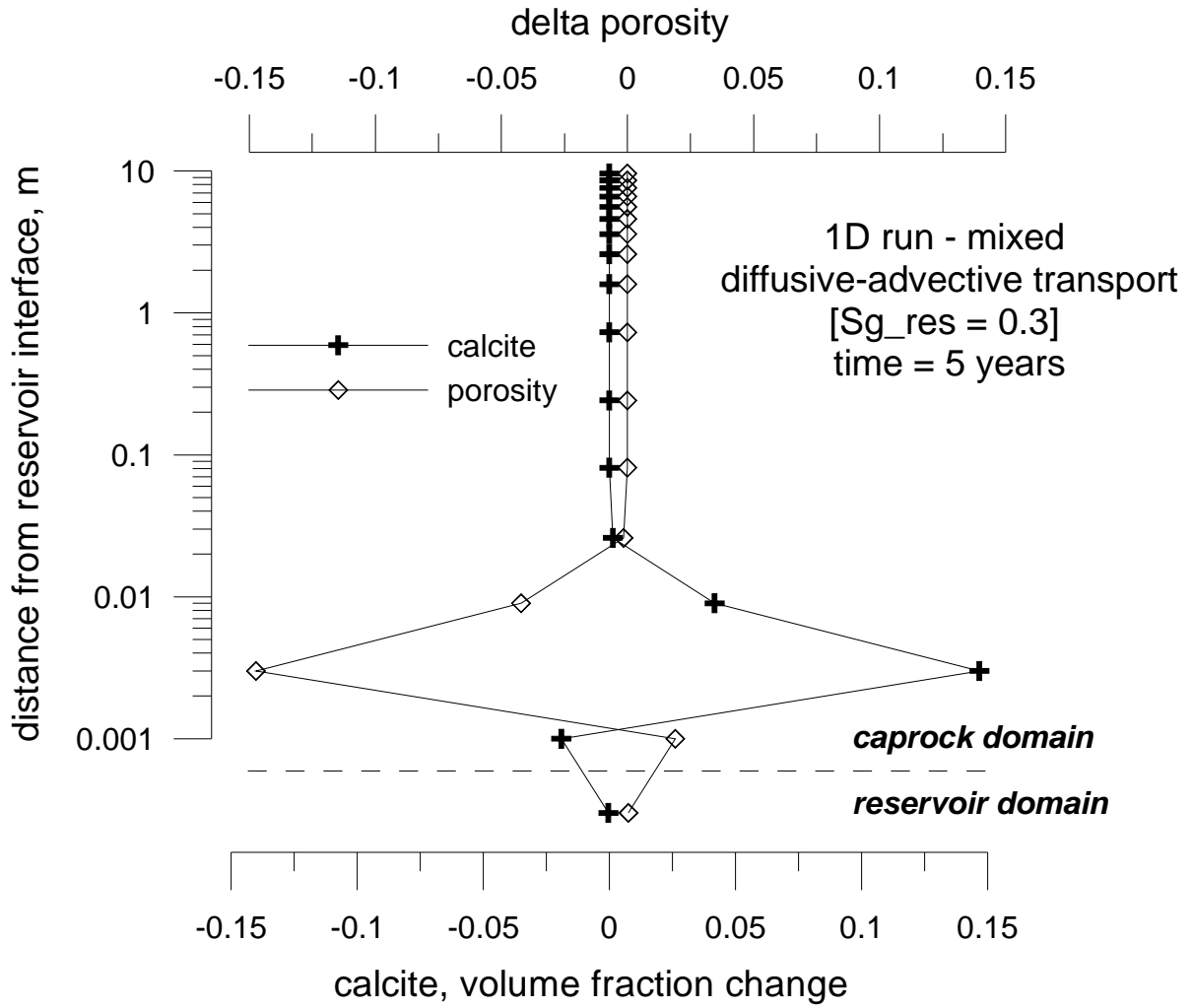


FIGURE 2

1D run - mixed diffusive-advective transport - [Sg_res = 0.30] - time = 5 years

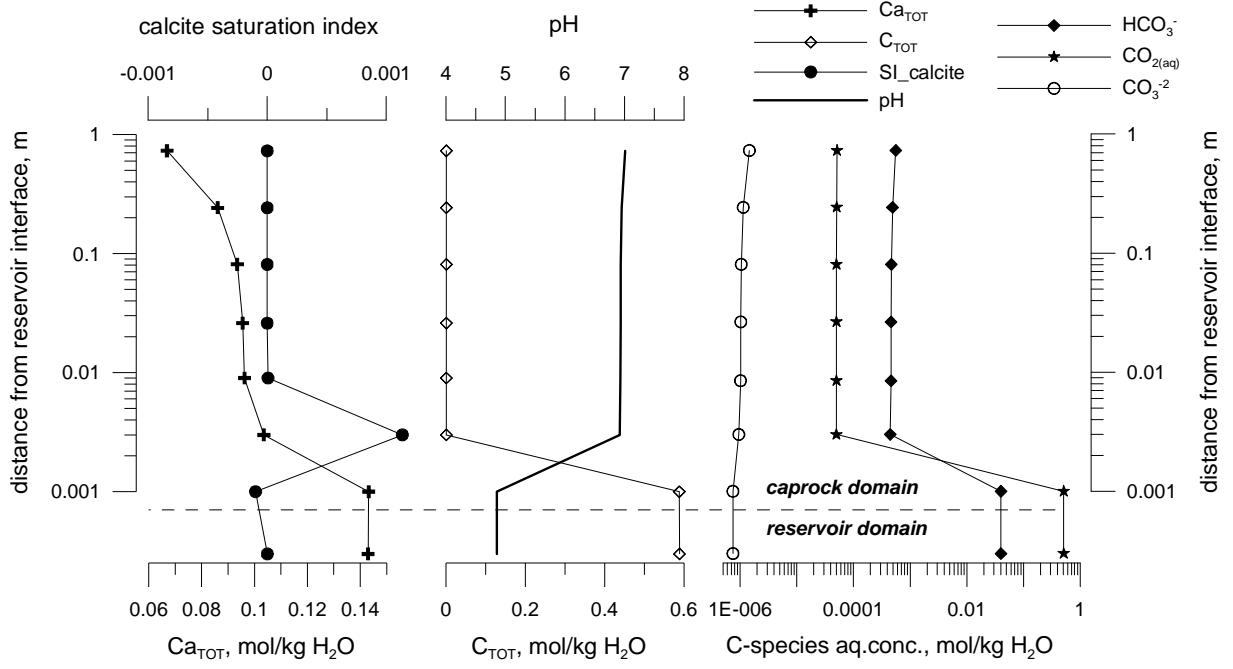


FIGURE 3

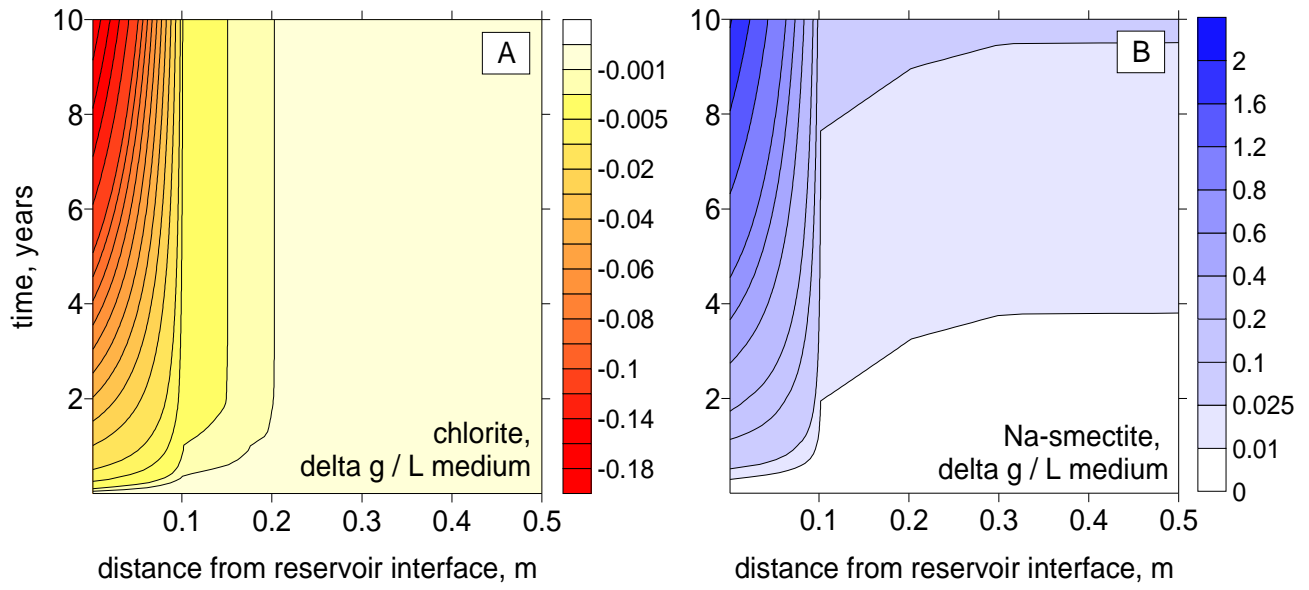


FIGURE 4

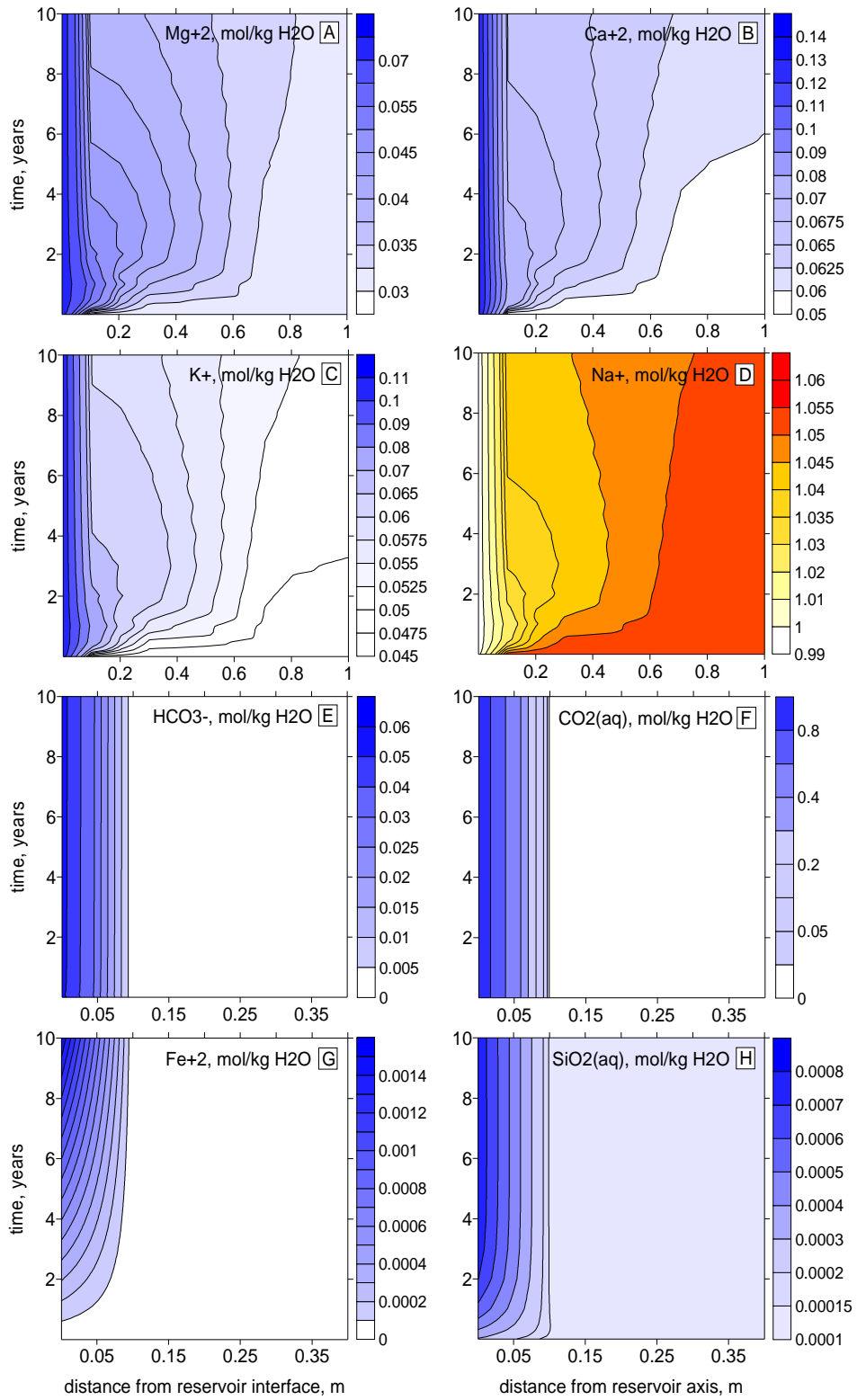


FIGURE 5

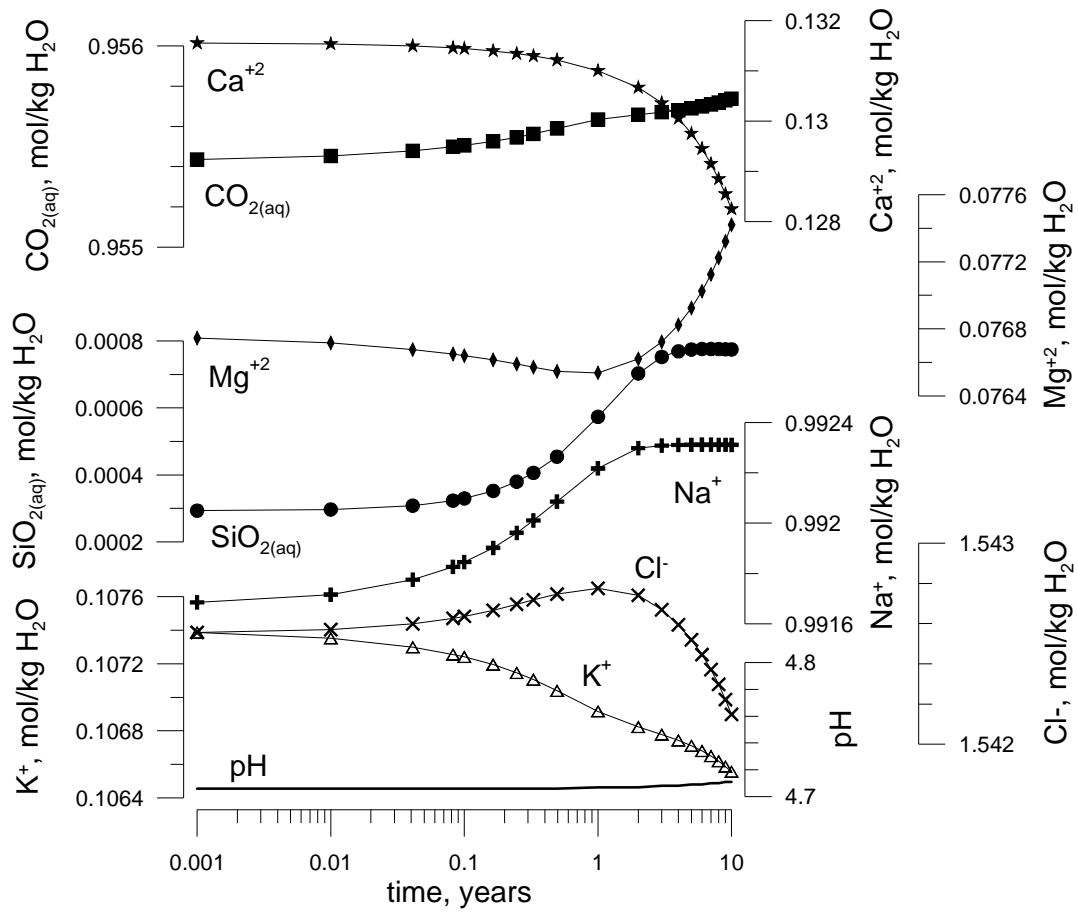


FIGURE 6

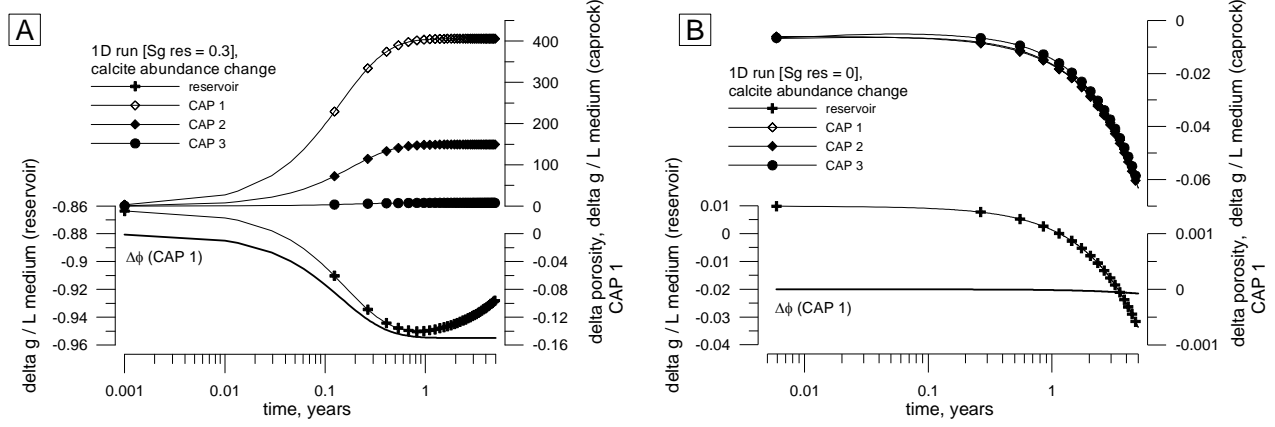


FIGURE 7

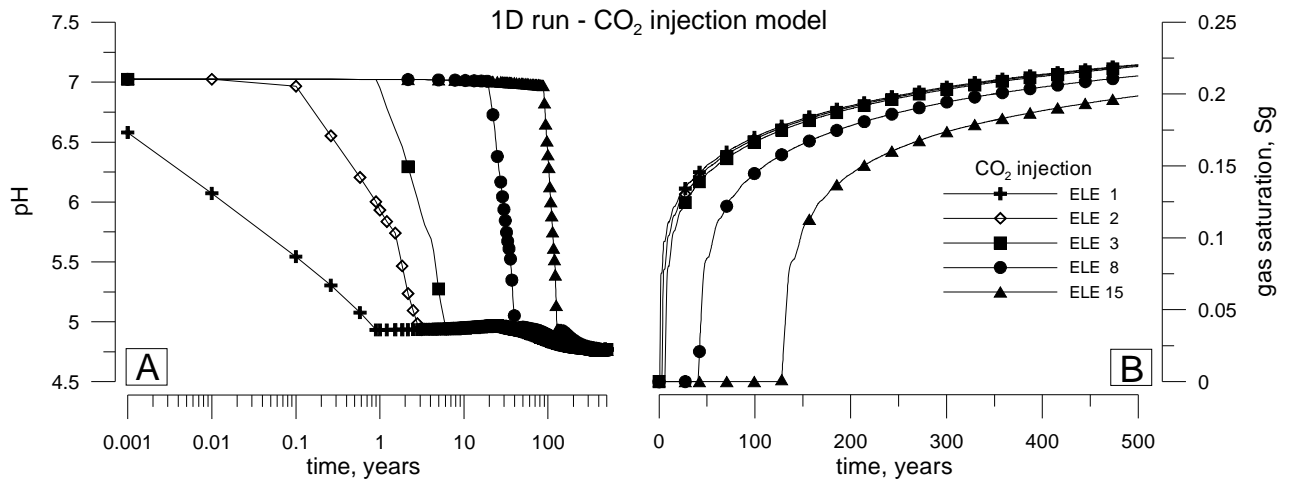


FIGURE 8

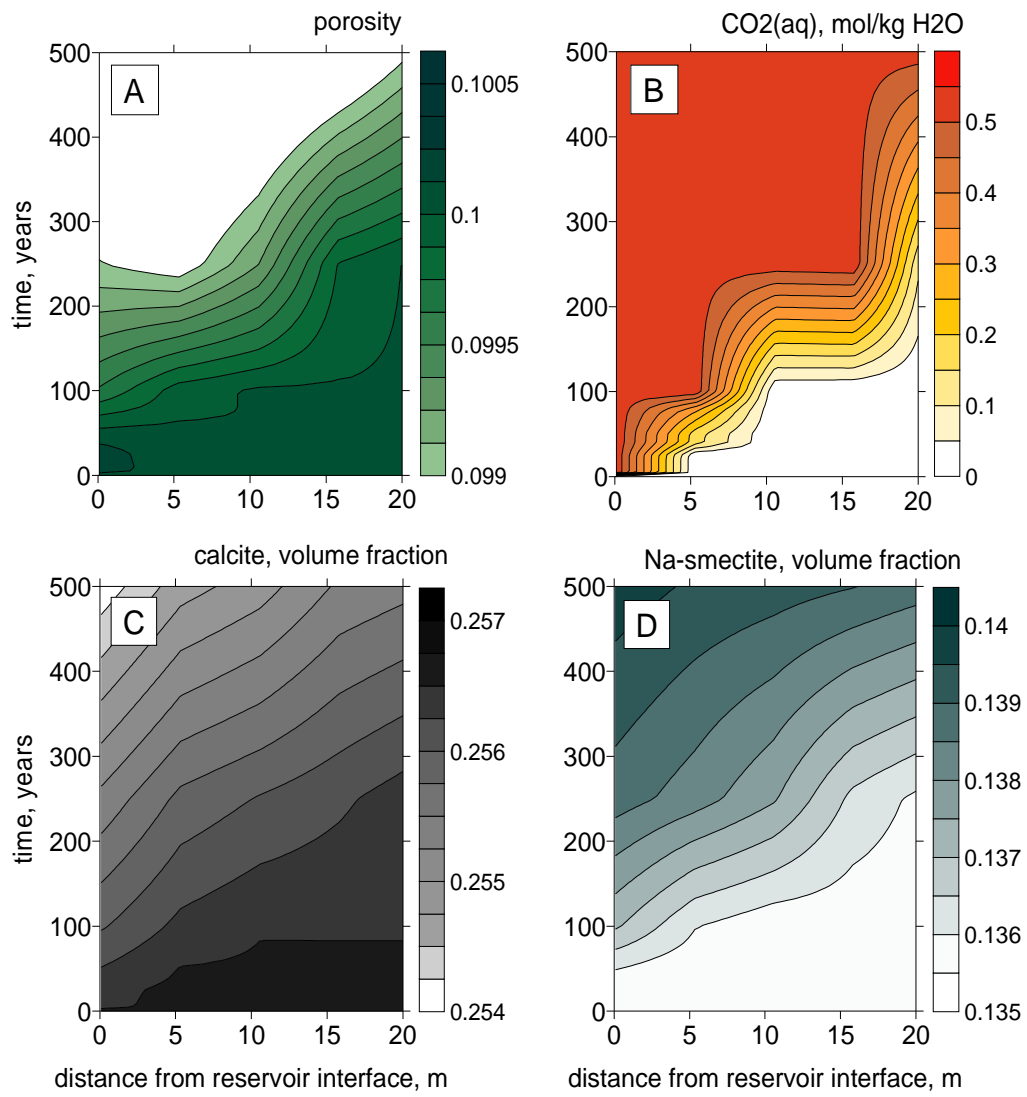


FIGURE 9

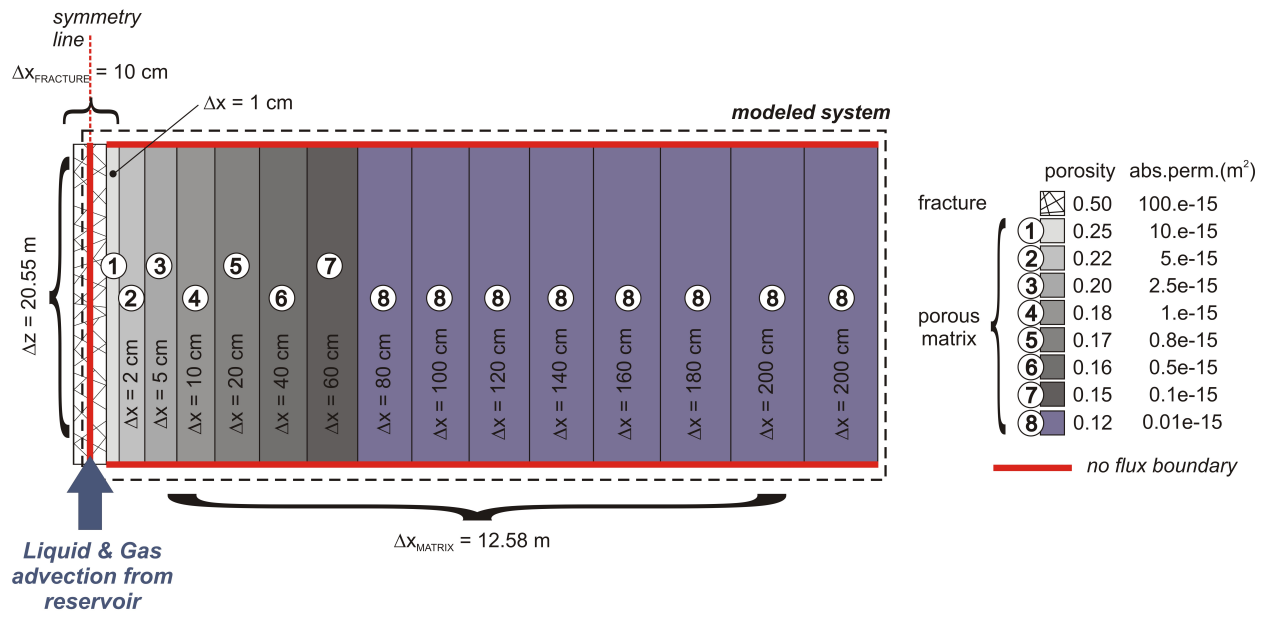


FIGURE 10

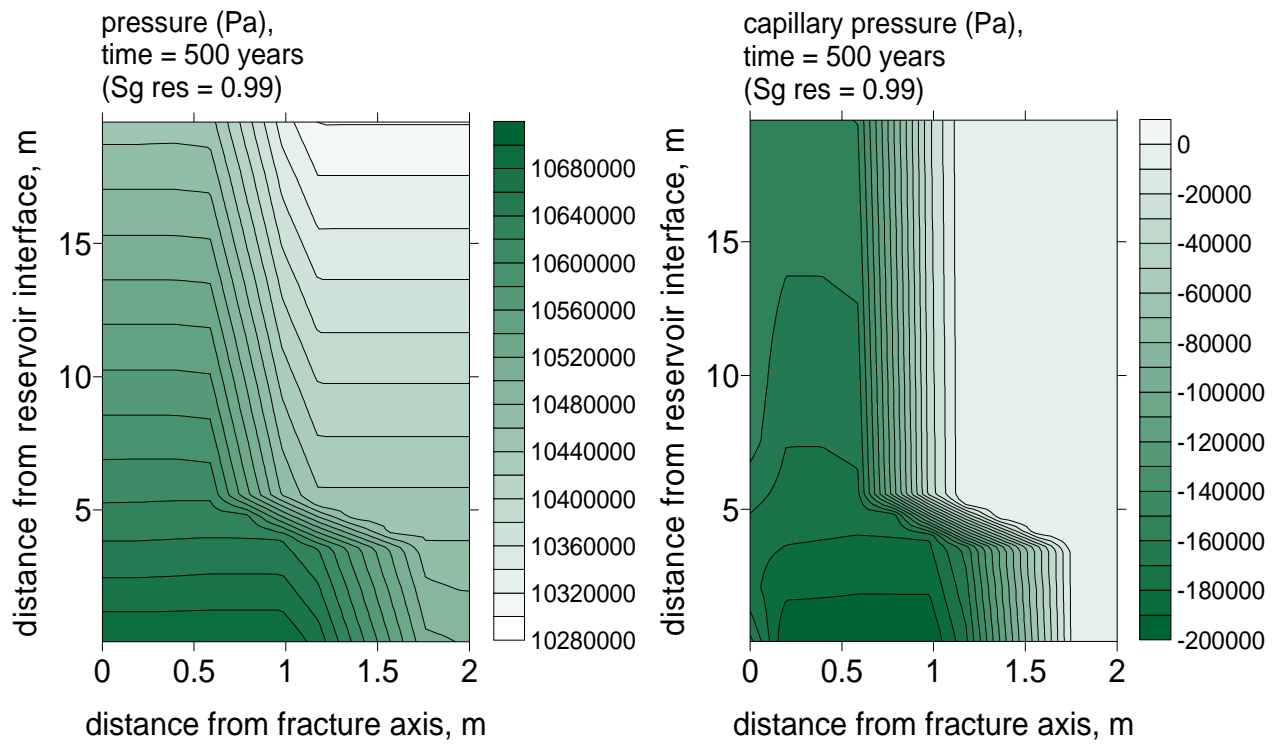


FIGURE 11

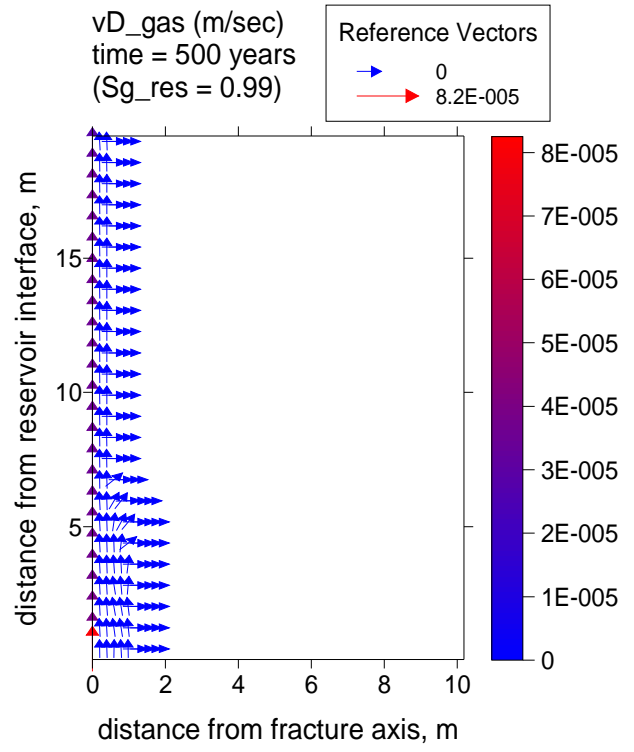
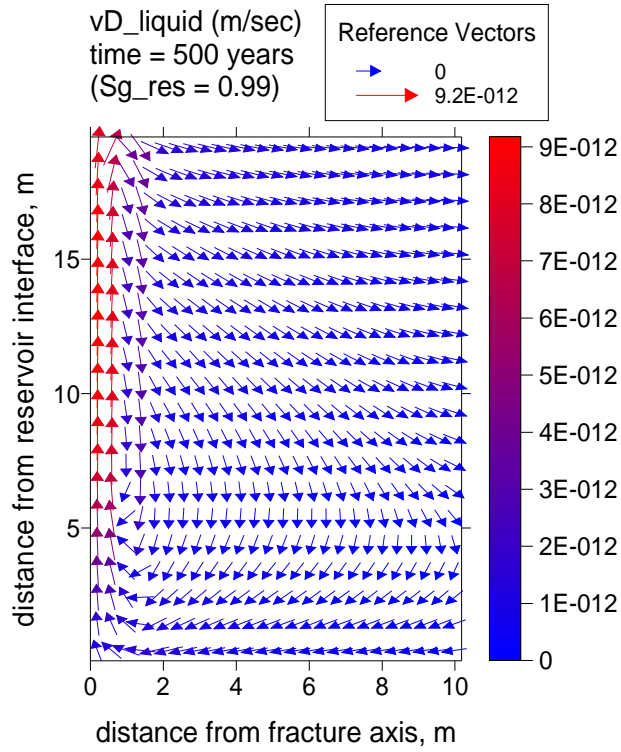


FIGURE 12

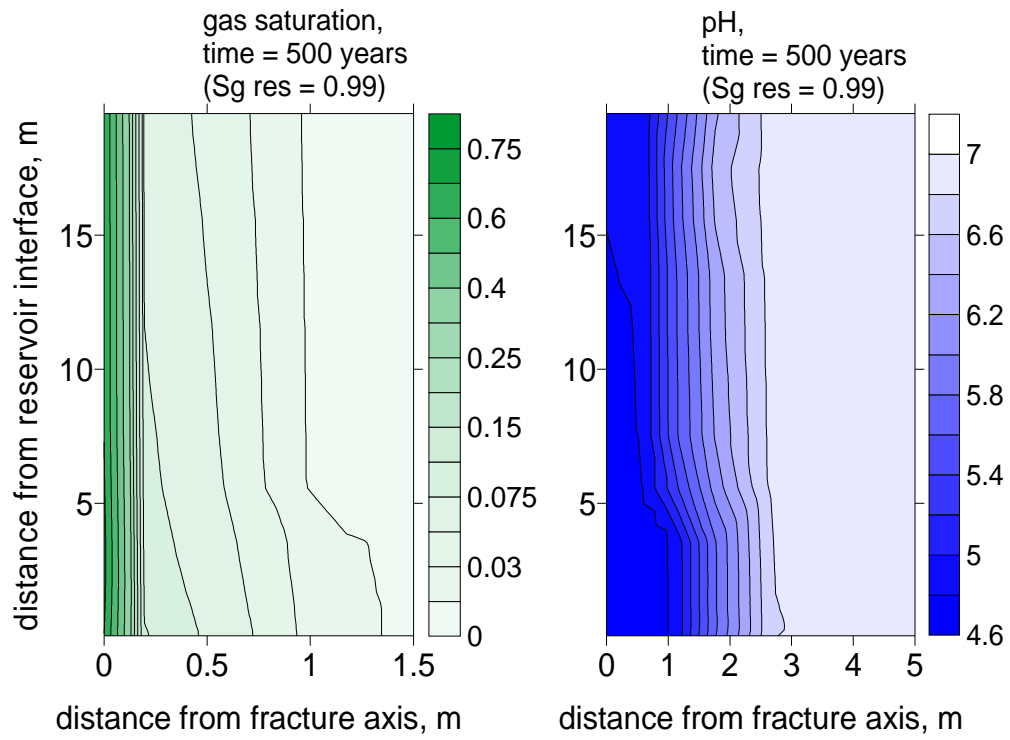


FIGURE 13

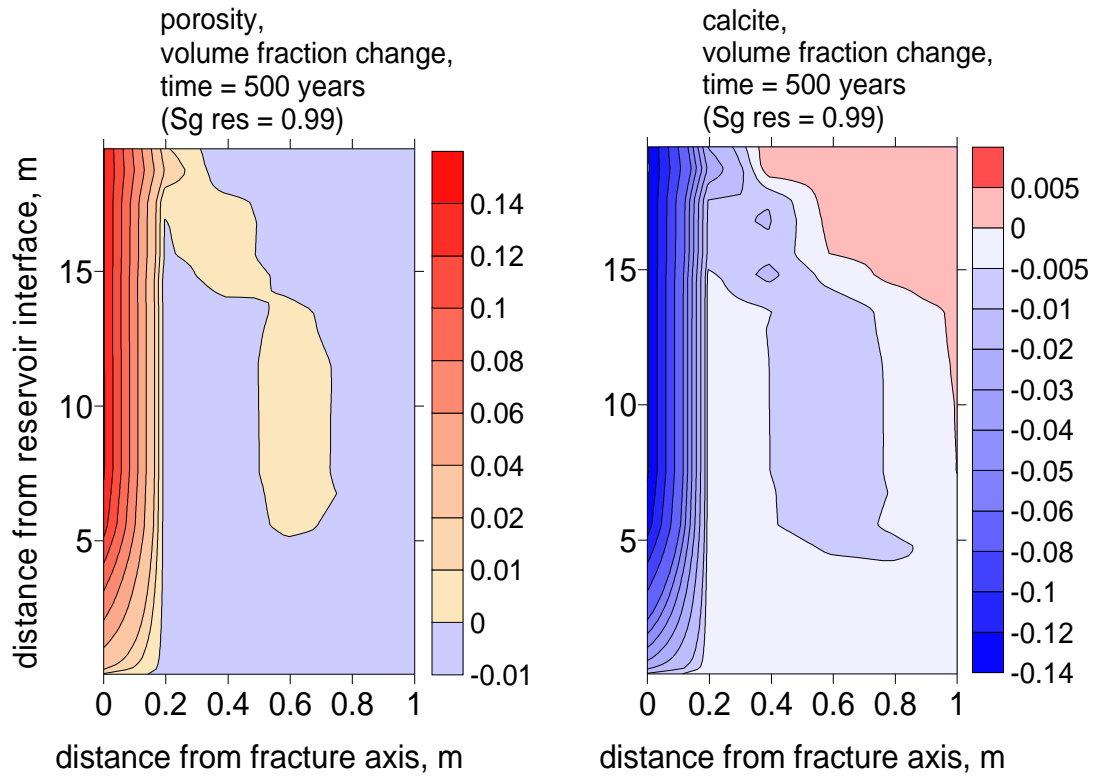


FIGURE 14

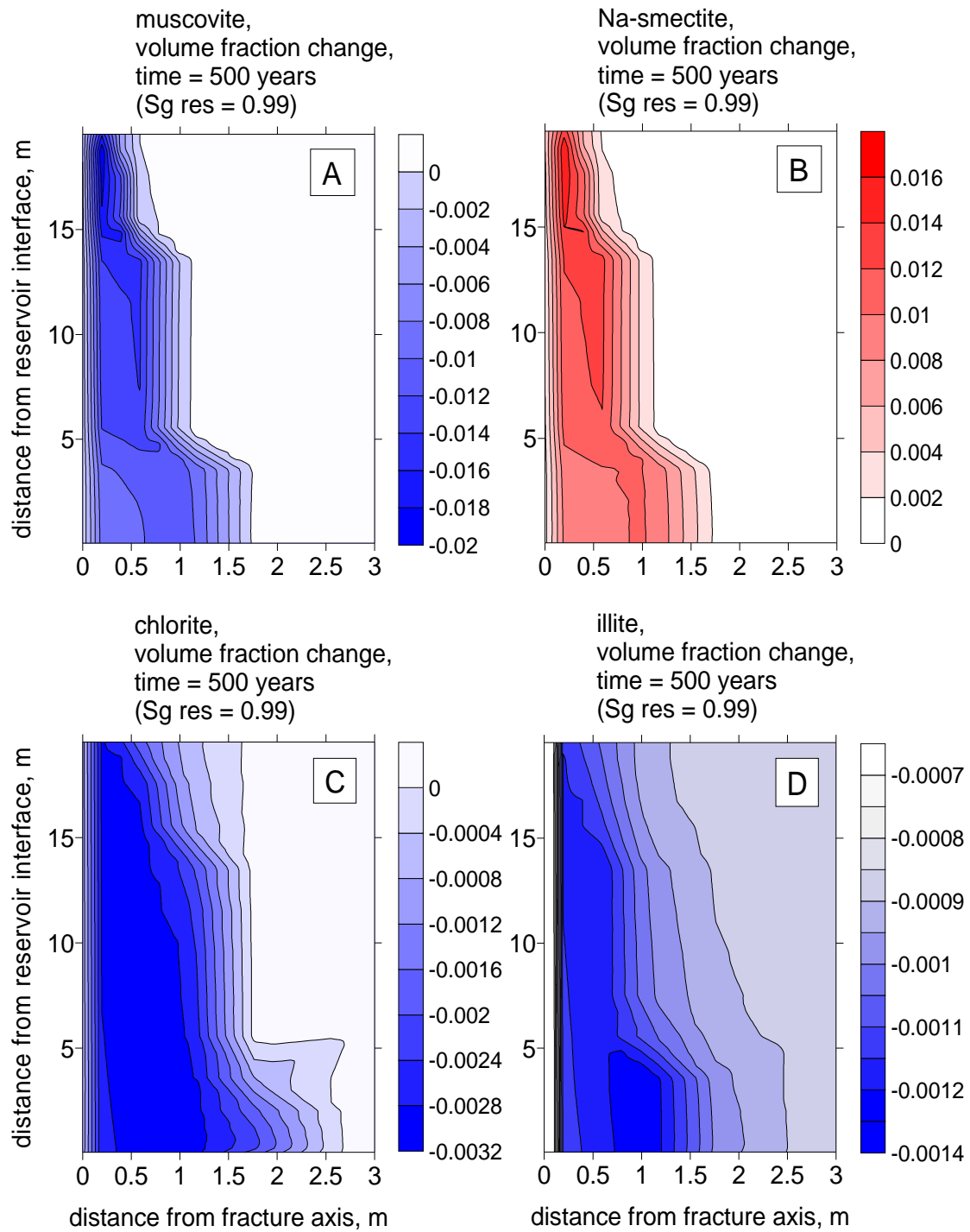


FIGURE 15

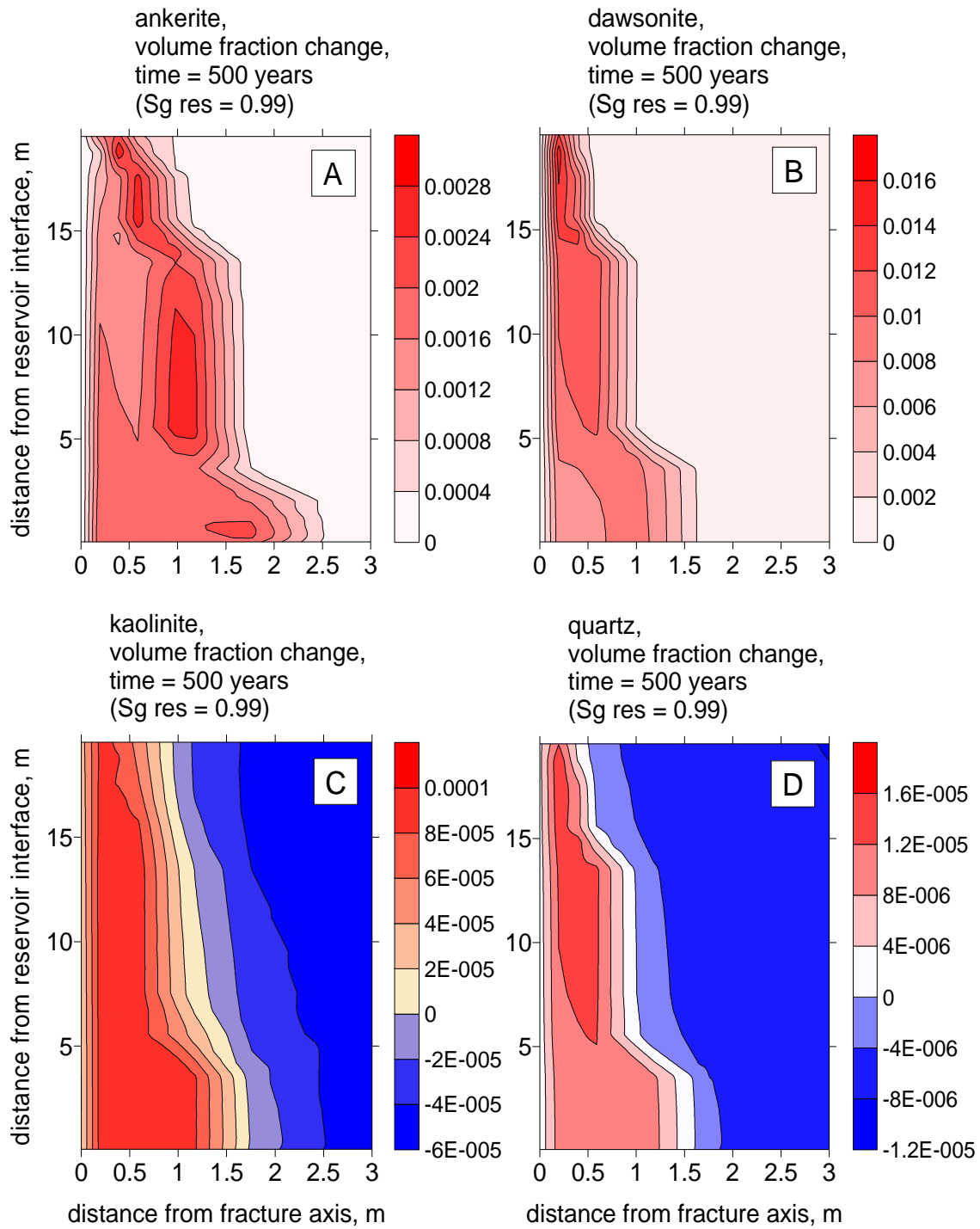


FIGURE 16

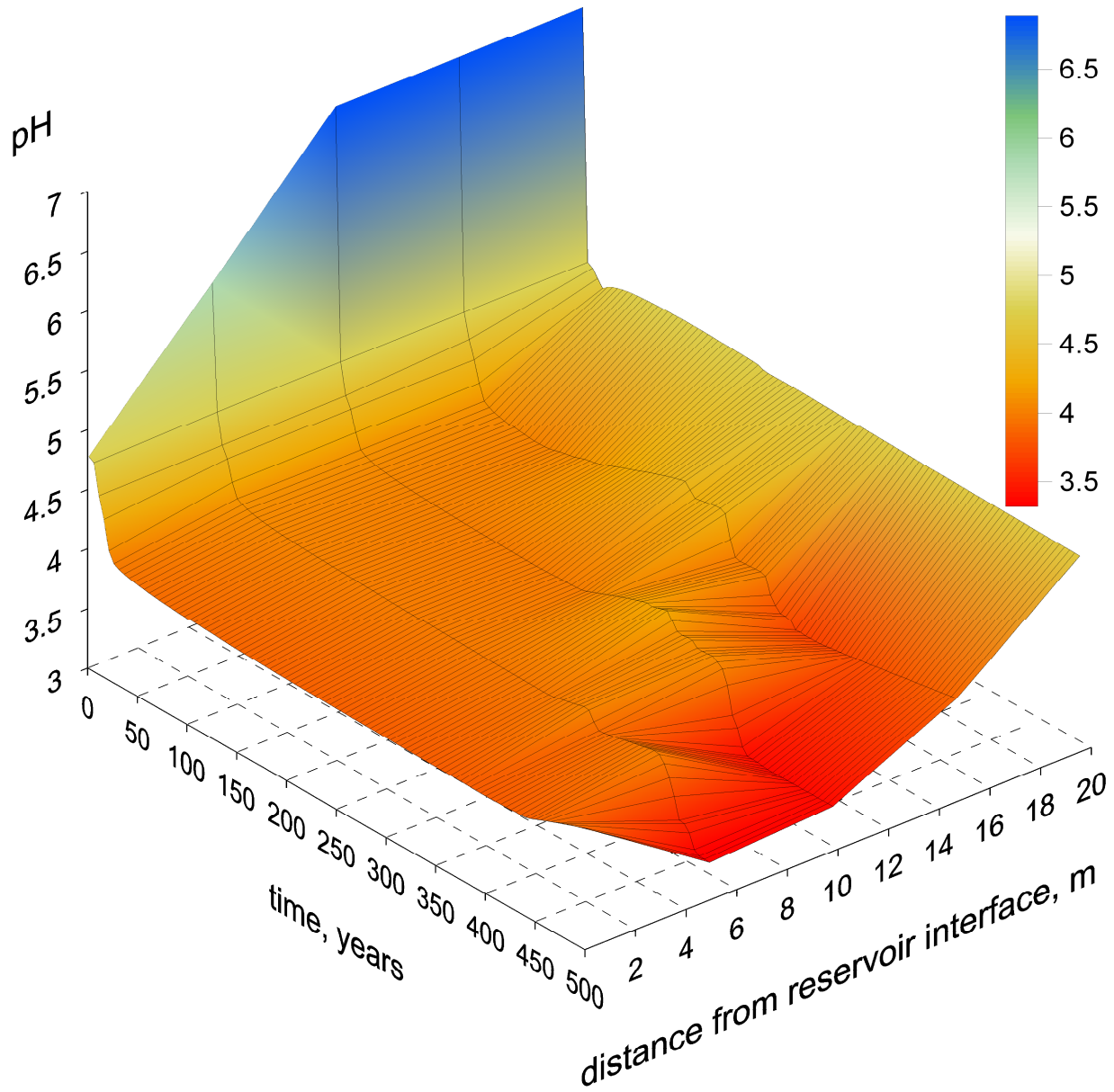


FIGURE 17

Table 1 – List of reservoir and caprock mineralogical compositions checked for sensitivity analysis (values in column: “Range”) and used for the “reference case” (column: “(Ref. case)”). Mineral abundances are expressed as volume fraction of solid.

Primary minerals	Reservoir		Caprock	
	Range	Ref.case	Range	Ref.case
Calcite	0.12 ± 0.04	0.12	0.30 ± 0.10	0.29
Dolomite	0.02 ± 0.02	0.04	0.03 ± 0.02	0.04
Quartz	0.35 ± 0.02	0.34	0.20 ± 0.05	0.20
Illite	0.03 ± 0.01	0.02	0.03 ± 0.01	0.02
K-feldspar	0.05 ± 0.02	0.05	0	0
Chlorite	0.09 ± 0.03	0.09	0.06 ± 0.02	0.06
Albite	0.15 ± 0.03	0.14	0	0
Kaolinite	0.02 ± 0.01	0.03	0.04 ± 0.02	0.05
Na-smectite	0.01 ± 0.01	0.01	0.15 ± 0.05	0.15
Muscovite	0.15 ± 0.05	0.16	0.20 ± 0.05	0.19

Table 2 – Details on water chemistry. *First two columns on the left:* chemical components and individual (primary and secondary) aqueous species (primary species in bold) considered in the calculations. *Last three columns on the right:* chemical composition of initial reservoir (analytical) and caprock (“synthetic”) pore waters (concentrations are in mol/kg H₂O; C_{TOT} are total concentration of component species).

Chemical components [§]	Individual aqueous species	Reservoir	Caprock
H₂O / <i>solvent</i>	H₂O , Ca⁺² , CaCl ⁺ , CaCl _{2(aq)} ,	T* = 23 °C	T = 45 °C
H⁺ / <i>pH</i>	CaCO _{3(aq)} , CaHCO ₃ ⁺ , CaOH ⁺ ,	pH = 5.90	pH = 7.48
Ca⁺² / <i>Ca_{TOT}</i>	CaSO _{4(aq)} , H⁺ , OH ⁻ , Mg⁺² ,		
Mg⁺² / <i>Mg_{TOT}</i>	MgHCO ₃ ⁺ , MgCO _{3(aq)} , MgCl ⁺ ,		
Na⁺ / <i>Na_{TOT}</i>	MgH ₃ SiO ₄ ⁺ , MgOH ⁺ , MgSO _{4(aq)} ,		
K⁺ / <i>K_{TOT}</i>	Na⁺ , NaCl _(aq) , NaCO ₃ ⁻ , NaHCO _{3(aq)} ,		
Fe⁺² / <i>Fe_{TOT}</i>	NaHSiO _{3(aq)} , NaOH _(aq) , NaSO ₄ ⁻ , K⁺ ,		
SiO_{2(aq)} / <i>Si_{TOT}</i>	KCl _(aq) , KSO ₄ ⁻ , Fe⁺² , Fe ⁺³ , FeCl ⁺ ,		
AlO₂⁻ / <i>Al_{TOT}</i>	FeHCO ₃ ⁺ , FeCO _{3(aq)} , FeCl ₄ ⁻² ,		
Cl⁻ / <i>Cl_{TOT}</i>	SiO_{2(aq)} , H ₃ SiO ₄ ⁻ , AlO₂⁻ , Al ₃ ⁺ ,		
HCO₃⁻ / <i>C_{TOT}</i>	HAIO _{2(aq)} , NaAlO _{2(aq)} , AlOH ⁺² ,		
SO₄⁻² / <i>S_{TOT}</i>	Al(OH) ₂ ⁺ , Cl⁻ , HCO₃⁻ , CO _{2(aq)} ,		
O_{2(aq)} / <i>redox</i>	CO ₃ ⁻² , CH _{4(aq)} , CH ₃ COOH _(aq) ,		
	SO₄⁻² , H ₂ S _(aq) , HS ⁻ , S ⁻² , O_{2(aq)}		
		Component	C_{TOT}
		Ca ⁺²	0.1092 × 10 ⁺⁰
		Mg ⁺²	0.1029 × 10 ⁺⁰
		Na ⁺	0.1154 × 10 ⁺¹
		K ⁺	0.1109 × 10 ⁺⁰
		Fe ⁺²	0.2328 × 10 ⁻⁴
		SiO _{2(aq)}	0.2923 × 10 ⁻³
		AlO ₂ ⁻	0.1000 × 10 ⁻⁷
		Cl ⁻	0.1720 × 10 ⁺¹
		HCO ₃ ⁻	0.2892 × 10 ⁻²
		SO ₄ ⁻²	0.1145 × 10 ⁻³
			0.7583 × 10 ⁻¹
			0.2458 × 10 ⁻¹
			0.1197 × 10 ⁺¹
			0.5133 × 10 ⁻¹
			0.3066 × 10 ⁻⁸
			0.1377 × 10 ⁻³
			0.2189 × 10 ⁻⁷
			0.1700 × 10 ⁺¹
			0.3631 × 10 ⁻³
			0.9988 × 10 ⁻⁶

[§] Chemical components are defined according to Reed (1982); parameters are reported according to the following notation: “name of chemical species” (in bold) “ / type of chemical constraint” (in italic)

* T is the temperature at which chemical analyses of reservoir pore waters were performed in the laboratory

Table 3 – Summary of minerals taken into consideration during the simulation and their kinetic constants ($k_{n,25}$), activation energies (E_a) and specific reactive areas.

Primary mineral	$k_{n,25}$ (mol/m ² /sec)	E_a (kJ/mol)	specific reactive area (cm ² /gr)
Calcite	1.6e-06	23.50	100e-1
Dolomite	3.0e-13	52.20	100e-1
Quartz	1.0e-14	87.70	100e-1
Illite	1.7e-13	35.00	1520e-1
K-feldspar	3.9e-13	38.00	100e-1
Chlorite	3.0e-13	88.00	200e-1
Albite	2.8e-13	69.80	100e-1
Kaolinite	6.9e-14	22.20	230e-1
Na-smectite	1.7e-13	35.00	1520e-1
Muscovite	3.0e-13	88.00	1520e-1

Secondary mineral	$k_{n,25}$ (mol/m ² /sec)	E_a (kJ/mol)	specific reactive area (cm ² /gr)
Pyrite	4.0e-11	62.76	130e-1
Ankerite	1.3e-09	62.80	100e-1
Oligoclase	1.4e-12	69.80	100e-1
Hematite	2.5e-15	66.20	130e-1
Magnetite	1.7e-11	18.60	130e-1
Magnesite	4.6e-10	23.50	100e-1
Siderite	1.3e-09	62.80	100e-1
Dawsonite	1.3e-09	62.80	100e-1
Ca-smectite	1.7e-13	35.00	1520e-1
Anhydrite	6.5e-04	14.30	100e-1
Halite	6.2e-01	7.40	100e-1
Anorthite	7.6e-10	17.80	100e-1

Table 4 - Initial values for selected physical parameters

Rock domain	rock grain density (kg/m ³)	porosity	kx, horizontal absolute permeability(m ²)	kz, vertical absolute permeability (m ²)
Reservoir	2720	0.325	400e-15	400e-15
Caprock	2830	0.15	0.1e-15	0.1 to 0.01e-15

<i>Capillary pressure, parameters for van Genuchten (1980) function</i>					
Rock domain	lambda	S _{lr}	S _{ls}	Pmax	1/P ₀
Reservoir	.457	.00	.999	1.e7	5.1e-5
Caprock	.457	.00	.999	1.e8	1.6e-7

<i>Liquid relative permeability, parameters for van Genuchten (1980) function</i>					
Rock domain	lambda	S _{lr}	S _{ls}	S _{gr}	
Reservoir	.457	.30	1.0	.05	
Caprock	.457	.30	1.0	.05	

Table 5 – 1D model grid specifications – 100 years simulation – order is from top to the bottom

Rock domain	Sub-domain	Number of elements	Thickness (m)	Node_d [§] (m)	Name of the element
Caprock	Layer 8	9	1.0	1.593 to 9.593	CAP 8 to CAP16
Caprock	Layer 7	1	0.729	0.7285	CAP 7
Caprock	Layer 6	1	0.243	0.2425	CAP 6
Caprock	Layer 5	1	0.081	0.0805	CAP 5
Caprock	Layer 4	1	0.027	0.0265	CAP 4
Caprock	Layer 3	1	0.009	0.0085	CAP 3
Caprock	Layer 2	1	0.003	0.0025	CAP 2
Caprock	Layer 1	1	0.001	0.0005	CAP 1
Reservoir	no subdomain	1	10.0	-	RES 1

[§] “Node_d” is the distance of the nodal point from reservoir-caprock interface (m)

Table 6 – 1D model grid specifications – 500 years simulation – order is from top to the bottom

Rock domain	Sub-domain	Number of elements	Thickness (m)	Node_d [§] (m)	Name of the element
Caprock	Layer 10	15	2.0	22.40 to 50.40	ELE26 to ELE40
Caprock	Layer 9	17	1.0	4.90 to 20.90	ELE 9 to ELE25
Caprock	Layer 8	1	0.9	3.95	ELE 8
Caprock	Layer 7	1	0.8	3.10	ELE 7
Caprock	Layer 6	1	0.7	2.35	ELE 6
Caprock	Layer 5	1	0.6	1.70	ELE 5
Caprock	Layer 4	1	0.5	1.15	ELE 4
Caprock	Layer 3	1	0.4	0.70	ELE 3
Caprock	Layer 2	1	0.3	0.35	ELE 2
Caprock	Layer 1	1	0.2	0.1	ELE 1
Reservoir *	no subdomain	1	10.0	-	RES 1

* A large volume (10^{+30} m^3) has been set to allows this domain to act as an almost infinite reservoir

§ “Node_d” is the distance of the nodal point from reservoir-caprock interface (m)

Table 7 – Average mineralogical composition (solid volume fraction) and porosity of upper and lower fracture domain compared with caprock initial values (data are after 500 years simulation). “Advection model”: a large, overpressurized reservoir almost completely filled with CO₂ (Sg = 0.99) set at the bottom of the caprock column forces the gas to move upwards; “Injection model”: CO₂ is directly injected into the bottom element of the caprock by means of an external source term.

Rock domain	phi %	cal %	dol %	qtz %	ill %	chl %	kaol %	Na-s %	musc %
initial	50.0	28.5	3.7	20.5	2.0	6.2	6.1	15.1	19.0
<i>Advection model</i>									
Upper fracture	64.2	0	5.1	28.6	2.8	8.4	7.2	21.8	26.1
Lower fracture	55.4	19.2	4.2	23.1	2.3	6.8	5.8	17.4	21.2
<i>Injection model</i>									
Upper fracture	63.7	0	0	29.9	2.8	8.5	7.5	22.9	22.2
Lower fracture	69.4	0	0	33.4	3.0	9.4	8.4	22.6	23.2

Abbreviations are as follows: phi=porosity; cal=calcite; dol=dolomite; qtz=quartz; ill=illite; chl=chlorite; kaol=kaolinite; Na-s=Na-smectite; musc=muscovite